© 2021. Published by The Company of Biologists Ltd | Development (2021) 148, dev192773. doi:10.1242/dev.192773

PRIMER

Inferring cell junction tension and pressure from cell geometry

Chloé Roffay[1,2,*,‡], Chii J. Chan[3,*,§,¶], Boris Guirao[2], Takashi Hiiragi[3,4] and François Graner[1,]**

ABSTRACT

Recognizing the crucial role of mechanical regulation and forces in tissue development and homeostasis has stirred a demand for *in situ* measurement of forces and stresses. Among emerging techniques, the use of cell geometry to infer cell junction tensions, cell pressures and tissue stress has gained popularity owing to the development of computational analyses. This approach is non-destructive and fast, and statistically validated based on comparisons with other techniques. However, its qualitative and quantitative limitations, in theory as well as in practice, should be examined with care. In this Primer, we summarize the underlying principles and assumptions behind stress inference, discuss its validity criteria and provide guidance to help beginners make the appropriate choice of its variants. We extend our discussion from two-dimensional stress inference to three dimensional, using the early mouse embryo as an example, and list a few possible extensions. We hope to make stress inference more accessible to the scientific community and trigger a broader interest in using this technique to study mechanics in development.

KEY WORDS: Mechanical stress inference, Cell junction tension, Cell pressure, Cell shape, Epithelia, Development

Introduction

The roles of mechanical interactions during morphogenesis, proposed more than one century ago (His, 1874; Thompson, 1917; Dupont, 2017), are now well recognized. Forces are generated by molecular motors, notably by actomyosin networks, and are transmitted via cytoskeletal elements through cell-cell adhesive complexes. Stresses (see Glossary, Box 1) are the effects of these internal forces, measured at the cell or tissue scale. Forces and stresses contribute to the determination of static cell shapes and packing (Graner and Riveline, 2017), as well as dynamic changes in cell size, shape, number and position, and gene expression, all of which ultimately contribute to tissue morphogenesis (reviewed by Heisenberg and Bellaïche, 2013; Heer and Martin, 2017). Reciprocally, tissue morphogenesis and mechanics can impact cell-fate specification (Gjorevski and Nelson, 2010; Mammoto et al., 2012; Chan et al., 2017). Such combined control by genetics and mechanics, and their feedback, helps to ensure that tissue development is simultaneously robust within a given species and variable across living organisms (Miller and Davidson, 2013; Hannezo and Heisenberg, 2019).

In vivo quantitative measurements of force and stress are therefore key to improving our understanding of how tissue morphogenesis is regulated. Recent years have seen technical inventions to measure force and stress (for reviews see Gjorevski and Nelson, 2010; Mashburn, 2015; Sugimura et al., 2016; Campàs, 2016; Roca-Cusachs et al., 2017; Gómez-González et al., 2020). Broadly speaking, these techniques belong to one of the following four classes: contact manipulation (e.g. parallel plate compression, atomic force microscopy and micropipettes); manipulation using light (e.g. optical tweezers and laser ablation); visual sensors (e.g. FRET sensors, liquid droplets and elastic beads); and non-mechanical observation techniques (e.g. birefringence and stress inference). These techniques measure either absolute or relative values of force or stress at various spatial and temporal scales, with various levels of precision, difficulty and cost. Whenever the same quantity can be measured by different methods, cross-validations can be performed. These methods are thus complementary and together constitute a useful toolbox.

Contact and light manipulation, as well as visual sensors, are somewhat invasive and typically provide mechanical information at a single location and time. Although one could consider constructing maps using single-point data from multiple experiments, biological variations often make such work impractical. In contrast, stress inference (see Glossary, Box 1) has gained popularity because it is inherently non-invasive, can provide information on multiple positions and time-points from a single experiment, and is also relatively cheap and fast. Thus, it is reasonably easy to implement with a high-throughput outcome, provided one has a high-quality image dataset that allows cell contours to be automatically segmented. It determines tensions and pressures in cells based only on image analysis, thanks to the following simple principle. When three cell junctions that meet at a vertex have an equal tension, by symmetry they meet at equal angles (i.e. 120°) (Taylor, 1976; Cantat et al., 2013; Graner and Riveline, 2017). Conversely, deviations from 120° angles indicate that junction tensions are different and the ratio of tensions can be calculated for these three junctions, then by iteration for all junctions of an individual cell, and even across a whole tissue. Similarly, the curvature of a junction between two cells is determined by the pressure difference between these cells; all pressure differences between cells can also be determined by the same logic.

Stress inference is a very promising approach to link mechanics and developmental processes, from the cellular to the tissue scale. In this Primer, we provide a beginner's guide to stress inference; our goal is to make the approach more accessible to the scientific community, especially for the non-specialists. We first recall the basic principles and underlying assumptions. We then review current two-dimensional (2D) variants with their respective strengths and limitations. We provide a practical checklist and

[1]Matière et Systèmes Complexes, Université de Paris - Diderot, CNRS UMR7057, 10 rue Alice Domon et Léonie Duquet, F-75205 Paris Cedex 13, France. [2]Polarity, Division and Morphogenesis Team, Genetics and Developmental Biology Unit, (CNRS UMR3215/Inserm U934), Institut Curie, F-75248 Paris Cedex 05, France. [3]European Molecular Biology Laboratory, 69117 Heidelberg, Germany. [4]Institute for the Advanced Study of Human Biology (WPI-ASHBi), Kyoto University, Kyoto 606-8501, Japan.
‡Present address: Department of Biochemistry, University of Geneva, Geneva 1211, Switzerland. §Present address: Mechanobiology Institute, National University of Singapore, 117411 Singapore. ¶Present address: Department of Biological Sciences, National University of Singapore, 117558 Singapore.
*These authors contributed equally to this work

**Author for correspondence (francois.graner@univ-paris-diderot.fr)

F.G., 0000-0002-4766-3579

Development (2021) 148, dev192773. doi:10.1242/dev.192773

Box 1. Glossary

Anisotropy. The property of a material to show variation in parameters along different axes. Here, the tissue stress anisotropy arises when cell junctions in different directions have a different tension distribution.

Bayesian method. Statistical method by which Bayes' theorem (Bayes and Price, 1763) is used to estimate the probability for a hypothesis to be true, within the constraints provided by all information available from other sources.

Coarse-graining. Obtaining a value of a quantity over a large spatial scale, by averaging the information available from a smaller scale.

Condition number. Mathematical quantity, which measures how truly independent the equations are. Here, a higher condition number indicates that a change or error in the measured angle and curvature values leads to larger changes in the inferred tension and pressure values. For further details, see supplementary information.

Inference. An approach based on induction, as opposed to deduction, adjustment or simulation. It consists in determining the input quantities (here stresses) that cause the observed data (here cell shapes) when a mathematical model describing their relationship is known.

Inversion. A mathematical operation performed during the process of inference. Here, it involves finding the inverse of a matrix.

Junction laser ablation. Using a focused laser to eliminate the molecular structures supporting the tension in a targeted junction. The opening velocity of the released junction immediately after ablation is proportional to the tension it had before ablation.

Mechanical equilibrium. The state when the net balance of forces on a system is zero. Here, a static state of epithelial tissues where in each cell-cell junction, tension and curvature balance pressure, and when junctions meet, their tensions sum up to zero vectorially. When this is not the case, a tissue is said to be out of equilibrium.

Relaxation time. The time taken for a viscoelastic material to significantly dissipate its internal stress when a constant strain (i.e. deformation) is applied to it.

Stresses. Mechanical forces exerted by a region of a material onto a neighbouring region, divided by the contact area between these regions. Cell stress can be coarse grained to yield tissue stress.

Tissue laser ablation. Using a focused laser to cut a line across several cells in order to measure the tissue stress perpendicular to this line. Alternatively, cutting a circular piece yields at once two tissue stress components.

Weissenberg number. The ratio between elastic and viscous forces in a viscoelastic fluid; equivalently, the product of relaxation time (which is a property of the material) and velocity gradient (which is a property of the flow).

Young-Laplace equation. This expresses that, at mechanical equilibrium, a deformable interface under tension has a curvature in direct relation to the pressure difference between the materials it separates.

flowchart to help the reader choose the appropriate variant, depending on the nature of the biological questions and on the available images. We also discuss recent developments in three-dimensional (3D) stress inference, its validations and limits, using the mouse embryo as an example to demonstrate and assess the pipeline. We conclude with some future perspectives, such as analysis of dynamic cell shape changes and extensions in 3D stress inference.

Stress inference: principle and application

The term 'force inference', which has often been used in the literature, could be considered misleading. Formally speaking, as Noll et al. (2020) argued, cell junction tension and cell pressure have no directionality, are not vectors, and are thus not forces. They are simply the components of the cell stress (Chiou et al., 2012). In this Primer, we use the term 'stress inference', and whenever necessary we specify the quantity being measured, by distinguishing 'cell junction tension', 'cell pressure' and their 'coarse-grained' (see Glossary, Box 1) version: the 'tissue stress'.

Using stress inference to study development

The idea of inferring cell stresses from images of cells within epithelial tissues was proposed long ago by Thompson (1917). To our knowledge, it was implemented for the first time by Stein and Gordon (1982). A froth made of soap bubbles is a well-known example of a pattern with equal tensions (Cantat et al., 2013). Analysing a five bubbles cluster, Stein and Gordon (1982) checked the tension values they inferred were equal within their precision, hence validating the approach. Using this approach, they further analysed a patch of 11 cells in the superficial cell layer of a frog gastrula and revealed significant differences among cell junction tensions.

In the 2000s, with progress in computers, live imaging and finite element modelling, Brodland and co-workers revisited this principle to infer tensions from cell shape images (Chen and Brodland, 2000; Brodland et al., 2007; Yang and Brodland, 2009; Cranston et al., 2010). In cases where limited information was sufficient to provide insights into the underlying cellular mechanisms, angles between cell junctions (Rauzi et al., 2008; Landsberg et al., 2009; Xiong et al., 2014; Samarage et al., 2015) or roughness of clone boundaries (Bosveld et al., 2016) were used as indicators of ratios of junction tensions, while cell junction curvatures were used as markers for cell pressure differences (Fujita and Onami, 2012; Lamiré et al., 2020). All these studies have contributed to the modern development of stress inference that we will now present.

Stress inference, as represented by its current variants discussed in this Primer, was first introduced by Chiou et al. (2012). It has been extensively used in two dimensions to obtain mechanical information mostly on planar epithelial tissues (Fig. 1, Table 1). In particular, it has provided important insights into the mechanics of *Drosophila* egg chamber formation (Bellver Arnau, 2015) (Fig. 1A), pupal dorsal thorax (Ishihara and Sugimura, 2012; Guirao et al., 2015) (Fig. 1B) and wing morphogenesis (Sugimura and Ishihara, 2013; Ishihara et al., 2013; Guirao et al., 2015); as well as embryo ventral furrow formation (Chiou et al., 2012), germband extension (Noll et al., 2020) (Fig. 1C,D) and germband retraction (McCleery et al., 2019). Stress inference has also been applied to study avian development, revealing tissue-scale pressure gradient in the quail primitive ectoderm (Kong et al., 2019) (Fig. 1E) and mechanical heterogeneity associated with hair-cell differentiation during avian cochlea formation (Chiou et al., 2012).

There have also been recent applications of stress inference to study 3D living tissues (Table 1). For example, during zebrafish gastrulation, stress inference revealed the influence of fluid osmolarity on tissue interfacial tension, and argued against the role of such tension in germ layer progenitor cell segregation (Krens et al., 2017). During blastoderm spreading in zebrafish, stress inference revealed a higher tension for the marginal deep cells compared with the central cells; this contributes to spatially patterned tissue fluidization (Petridou et al., 2019). In mice, stress inference revealed the role of tension gradient across cells to drive mammary gland tube elongation (Neumann et al., 2018). Stress inference has also been used to quantify tensions and pressures in early *C. elegans* embryo (Xu et al., 2018).

Underlying assumption of mechanical equilibrium

To be able to use stress inference, the tissue needs to be in mechanical equilibrium (see Glossary, Box 1); for exceptions to this

Development (2021) 148, dev192773. doi:10.1242/dev.192773

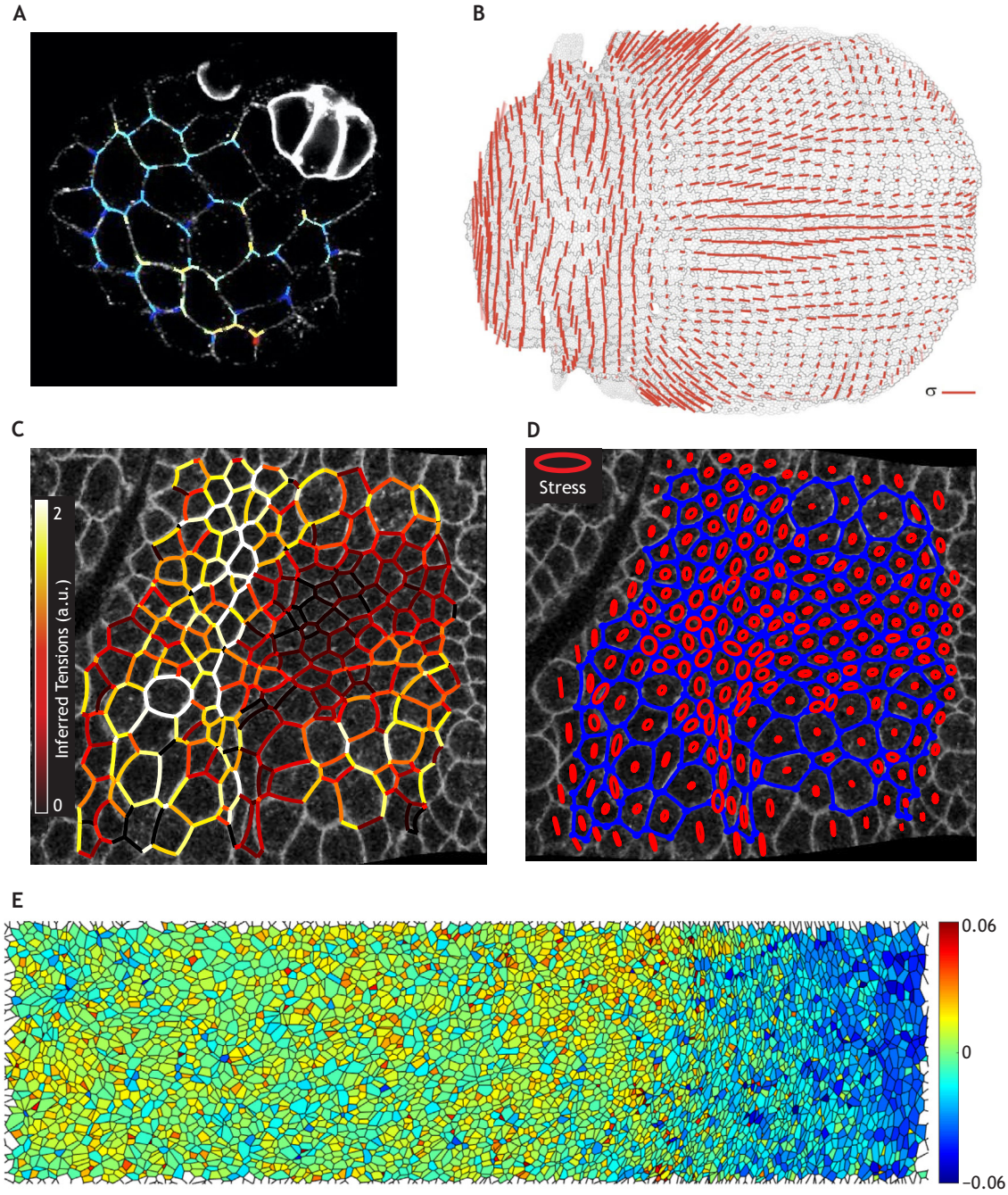

Fig. 1. Examples of stress inference in development. (A) Junction tension distribution in the *Drosophila* egg chamber. Confocal projection showing basal cell membranes and geometry of a group of three polar cells (bright) and neighbouring follicular cells on fixed tissue. Cell membranes are stained for Fas3, which is overexpressed in polar cells. Colours of follicle cell membranes indicate junction tensions relative to the average value of the entire tissue (from 0.58, blue, to 1.78, red). Picture courtesy of F. Agnès (Centre de Génétique Moléculaire, CNRS, France), analysis by J. Bellver Arnau (Bellver Arnau, 2015). (B) Map of tissue stress for the *Drosophila* pupal dorsal thorax. Adapted from Guirao et al. (2015), where it was published under a CC-BY 4.0 license. Each bar indicates the anisotropic part of tissue stress inferred from binned cell junction tensions. Bar direction indicates stress orientation; bar length indicates stress magnitude. (C,D) Overlay of color-coded inferred junction tensions (C) and inferred stress for each cell plotted as an ellipse (D) on a confocal image of the *Drosophila* lateral ectoderm near the cephalic furrow during late germ-band extension. Adapted from Noll et al. (2020), where it was published under a CC-BY 4.0 license. (E) Map of inferred pressures in the primitive ectoderm of a quail embryo. Adapted from Kong et al. (2019), where it was published under a CC-BY 4.0 license. Tensions, pressures and stresses are expressed in arbitrary units; cell sizes are not specified as they are not relevant for stress inference.

rule, see below ‘Dynamic stress inference’. The central hypothesis underlying stress inference is that cell shapes result from the balance of cell-cell interactions through junctions between two cells, and at vertices where the junctions meet. These interactions are mediated by two components acting perpendicular and parallel to the cell-cell junction. The magnitude of the perpendicular component acting on a junction between two cells is assumed to be determined by the difference in pressure between the cells. Each cell is assumed to have a homogeneous pressure and the pressure difference is thus assumed to be the same at all points along a given cell-cell junction. Similarly, the magnitude of the parallel component is assumed to be the cell-cell junction tension, homogeneous along the whole junction.

Development (2021) 148, dev192773. doi:10.1242/dev.192773

Table 1. Some applications of stress inference in living tissues

Biological systems	Results	Reference
Drosophila ventral furrow formation	Mechanical anisotropy at the onset of ventral furrow formation	Chiou et al. (2012)
Drosophila germband extension	Inferred cell stress predicts cell cleavage axis; validation of stress inference	Noll et al. (2020); Kong et al. (2019)
Drosophila germband retraction	Highly elongated shape of amnioserosa cells generates anisotropic tissue tensions	McCleery et al. (2019)
Drosophila egg chamber formation	Mechanical stress anisotropy does not play a role in triggering supernumerary polar cell apoptosis	Bellver Arnau (2015)
Drosophila pupal dorsal thorax metamorphosis	Tissue scale division pattern correlates with inferred junctional stress; validation of stress inference with laser ablation	Ishihara and Sugimura (2012); Guirao et al. (2015); Kong et al. (2019)
Drosophila pupal wing morphogenesis	Tissue stress along proximal-distal axis promotes hexagonal packing of cells	Sugimura and Ishihara (2013); Ishihara et al. (2013); Guirao et al. (2015)
Avian cochlea formation	Mechanical heterogeneity correlates with different cell fates during hair-cell formation	Chiou et al. (2012)
Early development of quail primitive ectoderm	Tissue-scale pressure gradient exists between embryonic and extraembryonic regions	Kong et al. (2019)
Blastoderm spreading in early zebrafish development	Mechanical heterogeneity contributes to tissue fluidisation	Petridou et al. (2019)
Gastrulation in early zebrafish development	Interfacial tension does not lead to spatial segregation of different germ cells	Krens et al. (2017)
Preimplantation development of mouse embryos	Validation of inferred tension with measurement by pipette aspiration	Veldhuis et al. (2017); supplementary information
Mouse mammary gland tube elongation	High tension in anterior protrusions and posterior tension gradient drives cell migration	Neumann et al. (2018)
C. elegans early development	Tension and pressure inference; sensitivity test on inference scheme	Xu et al. (2018)

There are many cases where this hypothesis is valid, at least approximately. In tissue morphogenesis, the cell contours are often static or ‘quasi-static’ (a slow succession of quasi-equilibrated states). Although stress inference has been extensively used to study living tissues, it has occasionally been applied to images of fixed tissues, as shown in Fig. 1A. Although the actual stress in the fixed sample is contributed by the polymerized proteins that maintain the tissue rigidity, the cell shapes should reflect the cell stress existing before fixation, so that stress inference is still valid.

Several approaches can be taken to decide whether a tissue resides close enough to mechanical equilibrium to perform stress inference. The first quantitative criterion is static. It can be applied either on a single image or on one frame of a movie. It consists of computing the left hand side of Eqn 1 (defined below) at each vertex, and checking that the right hand side is consistently close to zero. The right hand side is called the ‘residue’ of the equation. It is unlikely to be exactly zero for all vertex equations simultaneously. If the residues root mean square is much smaller than the average tension, then equilibrium hypothesis is reasonably valid. A similar criterion applies for Eqn 2 at each junction. The drawback of this static criterion is that it can be checked only *a posteriori*, after stress inference has been performed.

A second criterion, applicable only to live movies, is based on movements. The velocity gradient is a variation of local tissue velocity with respect to position, and is expressed as the inverse of a time. Multiplying it with the tissue relaxation time (see Glossary, Box 1), which could be measured independently [e.g. by tissue scale laser ablation (see Glossary, Box 1)], yields a dimensionless number known as the Weissenberg number (White, 1964) (see Glossary, Box 1). The Weissenberg number reflects the degree of anisotropy (see Glossary, Box 1) in deformation generated by the flow deformation rate. When it is less than one, the tissue has enough time to relax towards mechanical equilibrium, and is quasi-static; when it is larger than one, the tissue does not have time to relax and remains far from mechanical equilibrium.

In practice, however, a third and more qualitative criterion is used first to filter out tissues that are visibly far from mechanical equilibrium. Visual inspection often allows users, especially experienced ones, to detect deviations from equilibrium when they are large enough. For example, on a still image, sinuous junctions, very acute angles, protruding cells or triskelia (Fig. 2) imply that a set of tensions and pressures cannot suffice to explain the observed shapes. Several cell shapes are determined by junction resistance to bending. The shape of cells like axons or blebbing migrating cells are dominated by heterogeneous cytoskeleton forces. Since four- or fivefold vertices are rarely stable in tissues, an excessive proportion of such vertices probably reflects the existence of a mechanism which prevents their relaxation (Bardet et al., 2013). In all these cases, stress inference cannot be applied.

In a movie, excessive fluctuations of vertex positions or cell contours suggest that the tissue exists far from mechanical equilibrium. When a single image is available, it is impossible to distinguish whether cells undergo dynamical changes in time, or whether they are static due to ingredients other than tensions and pressures. In this Primer, for simplicity, we use the term ‘out of equilibrium’ in both cases without distinction.

In summary, larger or more numerous deviations from mechanical equilibrium, visible through cell shapes or through their fluctuations, imply a higher uncertainty of stress inference results. To decide whether it is worth applying stress inference, the user must compare the stress inference uncertainty with the precision required to answer the biological question. Where mechanical equilibrium conditions do not hold, see ‘Dynamic stress inference’ for an alternative option.

In practice: what stress inference can and cannot do

Given an image of epithelial cells, the possibility of using stress inference to obtain meaningful results depends on the scientific question under consideration and the objectives, which we discuss below. At each vertex, the ratio of junction tensions is measured (described in greater detail below), and inversion (see Glossary, Box 1) returns the ratio of each junction tension to the average tension within a given image. Each tension is

Development (2021) 148, dev192773. doi:10.1242/dev.192773

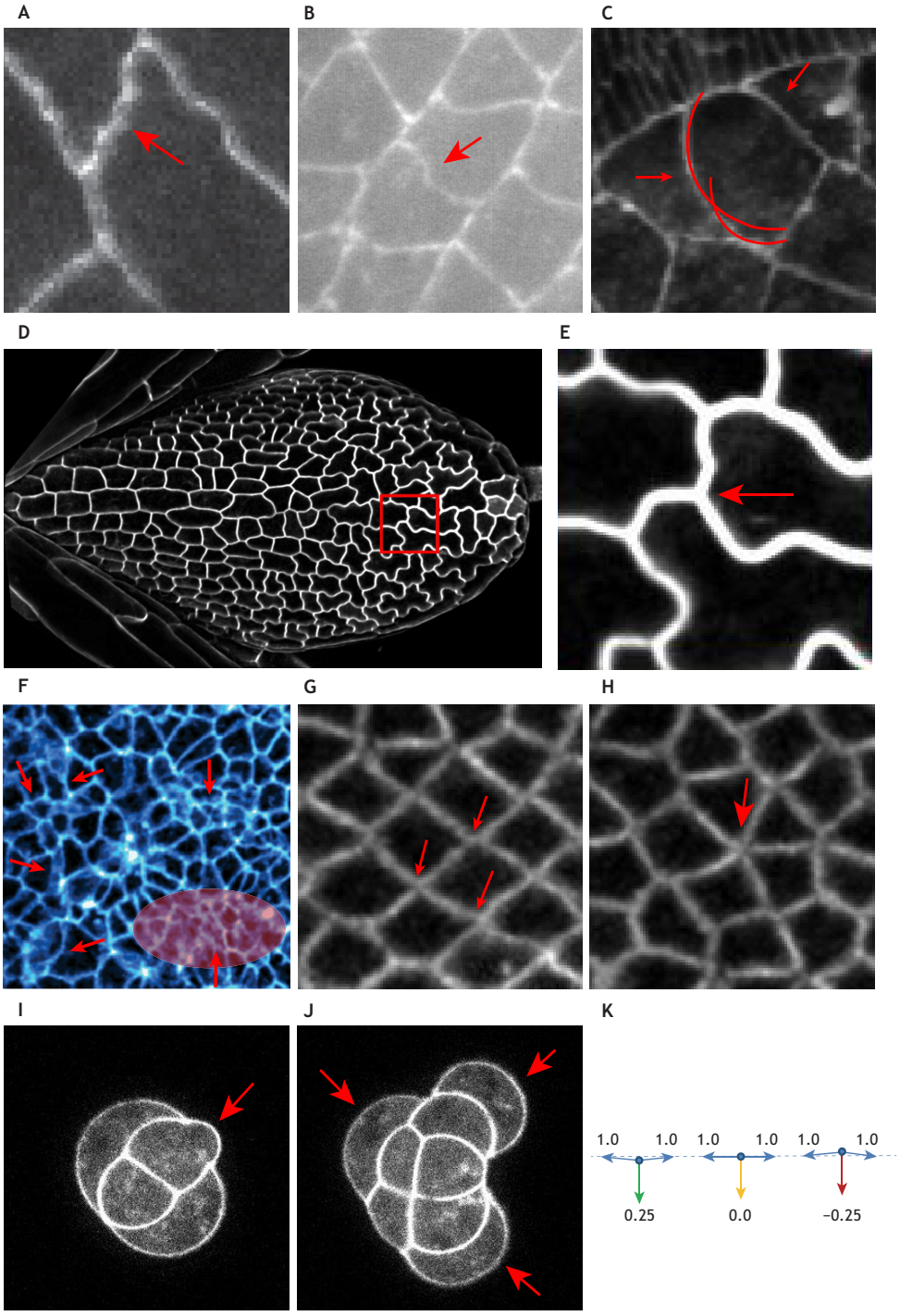

Fig. 2. Representative images of cell configurations that visibly deviate from mechanical equilibrium. This set is not exhaustive. Visible deviations are indicated by red arrows. (A) Crenellated edge, illustrated and discussed by Veldhuis et al. (2015). (B) S-shaped edge, illustrated and discussed by Kong et al. (2019). Adapted from Kong et al. (2019), where it was published under a CC-BY 4.0 license. (C) Edges with a constant sign of curvature but not a constant value (thus not a circular arc). Arrows indicate two such edges: on the left, the two different curvature radii are visualized; on the right, the arrow indicates the limit between a flat part and a curved one. (D) Plant tissue with very irregular cell shapes, illustrated by Carter et al. (2017). Most junctions are wiggly, similar to B. Red box indicates higher magnification of the region illustrated in E. (E) Triskelion: the curvatures of the three junctions that meet have the same sign. (F) Caco-2 colon epithelial cell monolayers whose cell-cell junctions are identified by endogenous E-cadherin tagged with GFP at its C terminus (Acharya et al., 2018). Arrows indicate some wiggly junctions; the ellipse marks a region where junction contrast makes segmentation difficult. Adapted, with permission, from Acharya et al. (2018). (G) Fourfold vertices meeting at nearly 90°, illustrated and discussed by Bardet et al. (2013). Some cases of fourfold vertices can be in stable equilibrium, see Spencer et al. (2017) and Kong et al. (2019). (H) Rosette-like fivefold vertex, illustrated and discussed by Bardet et al. (2013). G and H are adapted, with permission, from Bardet et al. (2013). (I,J) Early mouse embryos (see supplementary information). (I) Four-cell stage, with a bulging cell. (J) Eight-cell stage, with cells that cannot be fitted with a circular arc. (K) Schematic of angles ϕ around 180°, illustrated and discussed by Veldhuis et al. (2015); ϕ just below 180° (left) indicates one tension is much smaller than the others; ϕ equals 180° (middle) indicates a zero tension; ϕ just above 180° (right) would correspond to a negative tension (the junction pushes on the vertex), which is beyond the scope of stress inference methods. Cell sizes are not specified as they are not relevant for stress inference. A, C and K are adapted, with permission, from Veldhuis et al. (2015).

determined up to an unknown multiplicative constant, which is the same for all junctions in a given image. Hence, stress inference can map out spatial heterogeneity or anisotropy in junction tensions. With a movie, it can determine the fluctuations of tension ratios with time, but not how the tension in a given junction varies with time.

The sign of the pressure difference across a cell-cell junction is determined from the junction concavity. The pressure difference across the junction is calculated from its curvature and tension (Young-Laplace equation, see Glossary, Box 1). Hence, it is also determined up to the same unknown positive multiplicative constant as the tension. The inversion method returns the pressure in each cell, up to an unknown additive constant, so that the sign of the pressure itself is not determined and the pressure average can be set to zero. Stress inference can map out spatial heterogeneity in pressure and variation with time of relative pressure differences.

Stress inference is not based on any assumptions for the origin of the forces involved. Hence, in inferring the junction tension between any two cells, stress inference is not able to distinguish the relative contribution from each cell, nor from each biological ingredient, to the overall junction tension. For example, junction tension has been shown to increase with decreased cell-cell adhesion or increased cell contractility (Brodland, 2002; Ouchi

Development (2021) 148, dev192773. doi:10.1242/dev.192773

et al., 2003; Lecuit and Lenne, 2007; Käfer et al., 2007). To distinguish these antagonist contributions, stress inference is insufficient by itself, and should be used in combination with genetic or drug perturbations.

Stress inference results can be plotted as maps of pressures or tensions, histograms of tensions, polar plots of tensions versus direction (to determine tension anisotropy), graphs correlating each junction tension with another measurement in the same junction (for instance, protein distribution) or correlation between cell pressure and another measurement (e.g. cell size).

Let us discuss a practical example. In Fig. 2F, the experimentalist has identified a signalling pathway that responds when tensile stress is applied to epithelia. This involves the activation of Rho signalling; when that signalling fails, the epithelium fractures. Can stress inference capture the role of mechanical stress in this tissue?

This question needs to be subdivided. Are the assumptions for stress inference valid here? The bulk tissue appears to be in mechanical equilibrium, but a few cell contours are barely visible or appear wiggly, so stress inference may not be applicable to the entire tissue, and detection of mechanical heterogeneity is not possible. Can stress inference detect temporal variations of cell junction tensions due to activation of Rho signalling? No, stress inference can only indicate relative differences in tensions within a given image. Finally, can stress inference provide information on tissue stiffness and yield strength? No, such material properties have to be determined by other methods. Therefore, stress inference might turn useless to extract meaningful mechanical information for this particular biological question.

On the other hand, if there was a clone with high junction tensions (e.g. due to activation of actomyosin contractility), surrounded by a wild-type region with lower tensions, or if the aim was to detect a difference in tension between the junctions that fracture and those that remain intact, stress inference could be a valuable approach.

Two dimensional stress inference

In this section, we discuss 2D stress inference: its equations, variants, validations and choices to make in practice. The general framework for the stress inference pipeline has been described by Ishihara and Sugimura (2012). Readers interested in further details may refer to the 'Cellular Force-Inference Toolkit' (CellFIT) introduced by Brodland et al. (2014), for which the code is available online with several variants, or to Kong et al. (2019) for a more recent version.

Equations for mechanical equilibrium

For cell shapes, the mechanical equilibrium is quantitatively expressed using the two following rules (see Fig. 3 for notations

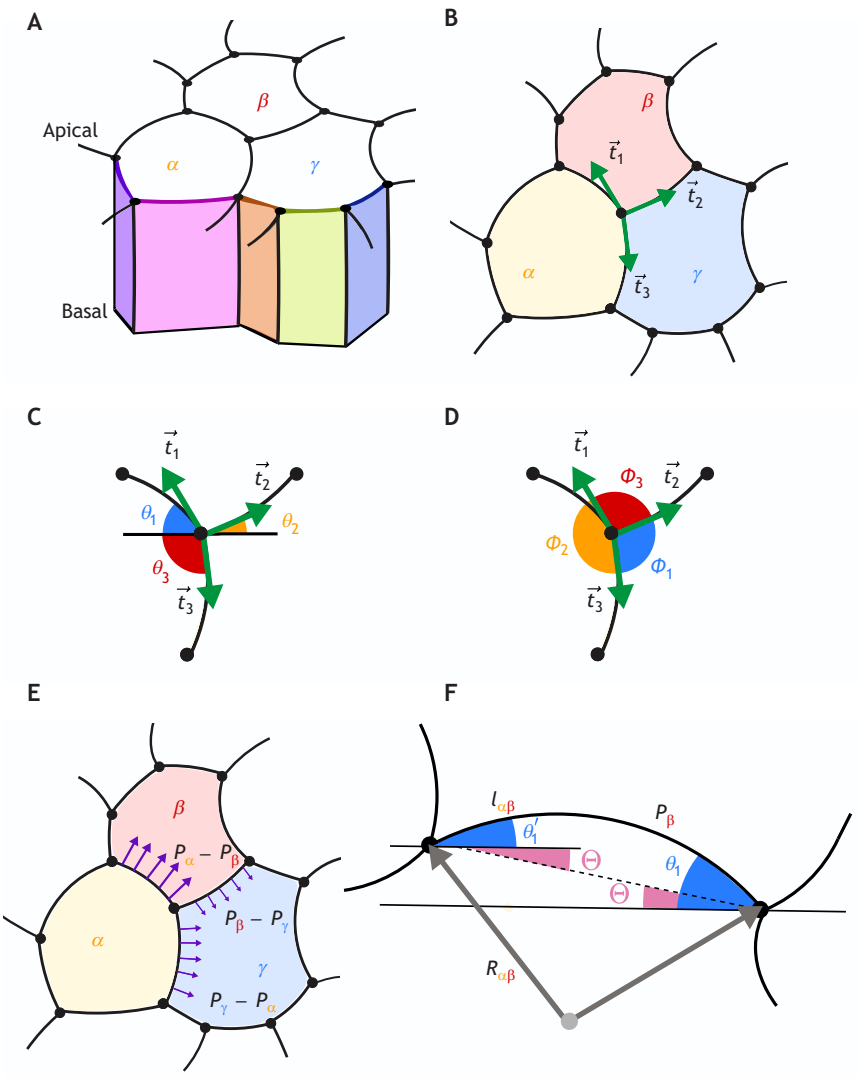

Fig. 3. Notations and principle of stress inference in two dimensions. (A) Each cell, labelled α, β or γ is apically constricted; cell shapes in the apical plane and in the basal plane are not necessarily identical. (B) In the two dimensional simplified description of the epithelium, only the adherens junction tension is taken into account. Each junction noted 1, 2, 3… is assumed to have a homogeneous tension t. (C) Representation of angles θ with the horizontal axis. The magnitude of tension is the same at both ends of the junction. (D) Representation of polar angles ϕ. (E) Each cell, labelled α, β or γ, is assumed to have a homogeneous pressure P. (F) A cell-cell junction is represented as a circular arc of radius R and a threefold vertex is where three cells meet or, equivalently, where three junctions meet. The angles θ and θ' of both arc ends with the horizontal axis are different. The chord is the straight line linking two adjacent vertices (dotted line). The angle Θ of the chord with the horizontal axis is the same at both its ends. Adapted from Noll et al. (2020), where it was published under a CC-BY 4.0 license. Drawings are schematics rather than equilibrium patterns.

Development (2021) 148, dev192773. doi:10.1242/dev.192773

and definitions). Readers may also refer to Graner and Riveline (2017) for further details.

The first rule expresses the mechanical equilibrium of a vertex in two dimensions. It states that the vertex is at rest when junction tensions $\vec{t}$, which are vectors, sum up to zero; e.g. for edges labelled 1, 2 and 3:

$$\vec{t}_1 + \vec{t}_2 + \vec{t}_3 = \vec{0}. \quad \text{(Eqn 1)}$$

The second rule, also known as the Young-Laplace equation, expresses the mechanical equilibrium of a junction between two cells. It states that each junction has a curvature K and tension t, which together balance the pressure difference between both cells, e.g. cells α and β:

$$\Delta P = tK. \quad \text{(Eqn 2)}$$

Here, $\Delta P = P_\alpha - P_\beta$; K is oriented from α towards β, i.e. is counted positively if α is the convex cell and β the concave one. Technically, pressures are in fact 2D pressures, expressed in Nm^{-1}; tensions are one dimensional tensions (also called line tensions) expressed in N; curvatures are expressed in m^{-1}. As a consequence of Eqn 2, each junction is smooth and has a homogeneous curvature K; in two dimensions, it is an arc of a circle with radius $R=1/K$.

This results in a set of mechanical balance equations: Eqn 1 at each vertex; Eqn 2 at each junction. In principle, this set of equations could be used for direct modelling. For example, in numerical simulations (Chiou et al., 2012; Ishihara and Sugimura, 2012; Ishihara et al., 2013; Brodland et al., 2014; Kong et al., 2019; Noll et al., 2020), the inputs are the tensions and pressures; implementing and solving the equations allows one to deduce the equilibrium cell shapes.

Here, the terms in the equations come from measurements based on image analysis. Stress inference, based on the same equations and assumption of mechanical equilibrium, acts as a kind of reverse engineering. Starting from the equilibrium cell shapes, it finds the cell junction tension and cell pressure. This is what 'inference' means, and technically this is achieved by 'inverting' equations.

Consequences of equations

These equations (Eqns 1 and 2) have at least four important qualitative consequences. A first consequence is a low proportion of fourfold vertices. A fourfold vertex (Fig. 4A, left) involves a larger total amount of junctional lengths than when it is decomposed into two threefold vertices (Fig. 4A, right) (Taylor, 1976; Cantat et al., 2013). In a particular tissue where all tensions are equal, the energy of a configuration would simply be the tension multiplied by the total amount of junctional length; the fourfold vertex would then cost more energy than two threefold vertices and be unstable. In the more general case of a tissue with unequal tensions, a fourfold vertex can sometimes be energetically stable (Spencer et al., 2017) but this is rare and most vertices are threefold.

A second consequence is the anti-correlation between angles and tensions. In the particular case where three junctions that meet had the same t, by symmetry they would necessarily form angles $\phi = 120°$ (Taylor, 1976). In the more general case of a tissue with unequal tensions, deviations from 120° increase when the tensions are increasingly different.

For example, in Fig. 3D, ϕ_2 is almost equal to 180°, and larger than ϕ_1 and ϕ_3. This indicates that t_2 is much smaller than t_1 and t_3. ϕ_1 is slightly smaller than ϕ_3 which indicates that t_1 is higher than t_3. This anti-correlation between angles and tensions is illustrated in more detail in Fig. 4B. Finally, junctions always meet at angles that

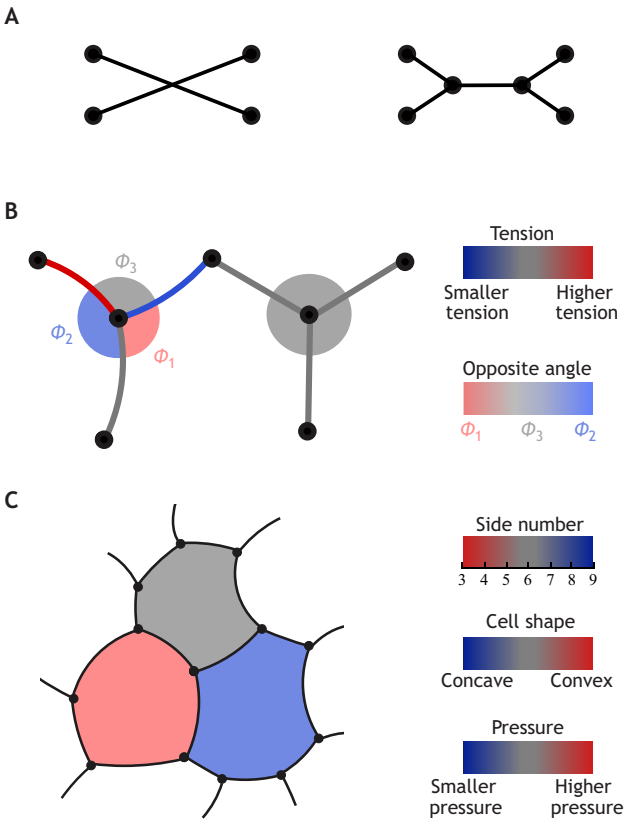

Fig. 4. General relationship between cell shape, tension and pressure in equilibrated tissues. (A) In an equilibrated tissue, a fourfold vertex (left) is rare; it involves a larger total amount of junctional lengths (Taylor, 1976; Cantat et al., 2013) than when it is decomposed into two threefold vertices (right), which are in the majority. (B) Illustration of the anti-correlation between angle and junction tension. Left: the angle ϕ_1 opposite a junction with high tension is small; the angle ϕ_2 opposite a junction with low tension is large, close to 180°. The angle ϕ_3 is intermediate and the opposite junction tension is also intermediate. Right: junctions with three equal tensions are balanced when they meet at 120° angles. (C) Illustration of the anti-correlation between side number and cell convexity. Cells with fewer sides tend to be more convex (and have a higher pressure) than their neighbours. Adapted from Noll et al. (2020), where it was published under a CC-BY 4.0 license. Drawings are schematics rather than equilibrium patterns.

are less than 180°; two junctions could meet exactly at 180° only if the third junction had zero tension (Fig. 2K).

A third consequence is the anti-correlation between side numbers and junction convexity. In a tissue where all junctions have the same tension, they would meet in three with 120° angles, as discussed above. Consider a cell in the interior of the tissue, surrounded by neighbours, with five sides or fewer. To close this cell while simultaneously meeting at 120°, for purely geometrical reasons at least some junctions must be convex (bent outwards). For the same geometrical reasons, cells with seven sides or more have junctions that are mostly concave (bent inwards). Cells with six sides have junctions with an average curvature near zero; they can, but need not have flat junctions (Fig. 4C). This is related to pressure difference because, according to Eqn 2, a cell that has a convex junction with one of its neighbours has a higher pressure than this neighbour (Cantat et al., 2013).

In the more general case where junction tensions differ, this relation between convexity and side number still holds approximately true. Larger tension differences imply larger deviations to this

Development (2021) 148, dev192773. doi:10.1242/dev.192773

relation, but broadly speaking, the smaller the side number of a cell, the more concave are its junctions and the higher its pressure with respect to its neighbours (Fig. 4C).

A fourth consequence is that three junctions that meet cannot all be bent in the same direction as in Fig. 2E. To express it quantitatively, when three cells meet at a vertex, e.g. α, β and γ in Fig. 3, one can start from cell α, run around the vertex by crossing to β, then γ, and come back to cell α. Summing the pressure differences across the three junctions 1, 2 and 3 encountered in this route, one can trivially write that $(P_\alpha - P_\beta) + (P_\beta - P_\gamma) + (P_\gamma - P_\alpha) = 0$. So the consequence of Eqn 2 is that the sum of tKs (product of junction tension and curvature) over the three junctions is zero:

$$t_1 K_1 + t_2 K_2 + t_3 K_3 = 0. \qquad \text{(Eqn 3)}$$

Hence, their curvatures K_1, K_2 and K_3 cannot all have the same sign.

In the particular case where all three junctions have the same t, the sum K_1+K_2+K_3 of their curvatures would be zero (Cantat et al., 2013). In the more general case where tensions differ, this approximately holds true and the sum of their curvatures is small.

Solving the equations

To determine all tensions, Eqn 1 is written for each vertex. To determine all pressures, Eqn 2 is written for each junction. This results in a large system with many unknowns and equations. In a tissue made of N cells, which mostly meet by three, the number of vertices is around $2N$ and the number of junctions is around $3N$. This results from simple counting: it is independent of both the nature of the tissue and the type of packing, whether hexagonal or not (Graner and Riveline, 2017).

The polar coordinates using angles ϕ, which Figs 3D and 4B show for pedagogical explanations, are seldom used in practice (see 'Extensions'). Rather, Eqn 1 is projected on horizontal axis x and on vertical axis y, so there are still two equations per vertex, in cartesian coordinates. All equations are then solved simultaneously to find the tensions and/or the pressures.

The resolution method depends on the number of equations and unknowns. This in turn depends on what can be feasibly measured: chord angles or tangent angles? Is curvature measurable? It also depends on what one is looking for: tensions only, or tensions and pressures? Accordingly, the literature offers four variants of stress inference (Fig. 5). We now examine them one by one.

Four variants of stress inference

For biological questions where the knowledge of cell pressures is not needed, curvature measurement is not required. The first two variants do not consider curvature.

Chord tension inference

The first variant [called mechanical inference by Mashburn (2015)] is what we call chord tension inference. It considers actual vertices but approximates the actual junctions as straight lines between vertices; i.e. it replaces each junction with its chord, angles θ of the junction (with respect to horizontal x axis) with angle Θ of the chord (Fig. 3F), and each cell with a polygon (Chiou et al., 2012). This is acceptable when junctions are almost straight and pressures are assumed to be almost identical. The measured quantities are the angles Θ. The unknown quantities are the tensions. Their number is one tension per junction, that is, $3N$, up to boundary cells; while the number of equations, based on Eqn 1, is two per vertex:

$$\begin{aligned} t_1 \cos\Theta_1 + t_2 \cos\Theta_2 + t_3 \cos\Theta_3 &= 0, \\ t_1 \sin\Theta_1 + t_2 \sin\Theta_2 + t_3 \sin\Theta_3 &= 0. \end{aligned} \qquad \text{(Eqn 4)}$$

i.e. $4N$ up to boundary cells. Hence, for a large enough tissue, where the bulk cells largely outnumber boundary cells, there are many more equations than unknown quantities. The problem is called 'overdetermined', which means its resolution is simple and robust. A usual matrix inversion code yields the values of the unknown that satisfy best (but not perfectly) all equations simultaneously. Each fourfold vertex reduces the ratio of equations to unknown quantities (two equations for four junctions, instead of two for three) and this renders the problem less overdetermined; fivefold vertices reduce even further the overdetermination.

When many cells are considered, the number of equations and unknowns is large; the inversion code needs to be accelerated. As each equation concerns only few junctions, so-called 'sparse matrix' methods can be used, as foreseen by Stein and Gordon (1982). For experienced users, we refer to Kale et al. (2018), who have implemented a useful technical improvement that they call 'variational mechanical inference'.

Tangent tension inference

The second variant, which we call tangent tension inference, uses more precise input data, so that the outputs are also more precise (Brodland et al., 2014). The number of equations is the same as in chord tension inference but it instead uses the angles θ_i, θ'_i of actual tangents at both ends of the junction with the horizontal x axis (Fig. 3C,F). Eqn 1 becomes:

$$\begin{aligned} t_1 \cos\theta_1 + t_2 \cos\theta_2 + t_3 \cos\theta_3 &= 0, \\ t_1 \sin\theta_1 + t_2 \sin\theta_2 + t_3 \sin\theta_3 &= 0. \end{aligned} \qquad \text{(Eqn 5)}$$

Curved junction stress inference

When the knowledge of cell pressure is needed, the third variant [called cellular force-inference toolkit in Mashburn (2015)] is what we call curved junction stress inference. It measures junction curvature to determine pressures using Eqn 2: the number of equations is then $6N$ (Brodland et al., 2014). The simplest way is to determine first the tensions using tangent tension inference, and then use these tensions to determine pressures (Veldhuis et al., 2015). As the number of pressures is equal to N, the total number of unknown quantities (tensions and pressures) is $4N$, up to boundary cells.

Several improvements are possible. First, based on arc length ℓ (Fig. 3F), Eqn 2 can be rewritten using the integrated form $\Delta P\ell = t_i(\theta_i - \theta'_i)$, and estimating ℓ could be more robust than measuring the curvature.

Second, Brodland et al. (2014) present a more precise (and more computationally intensive) procedure that simultaneously determines tensions and pressures.

Third, all variants discussed so far consider individual static images; where a time-lapse movie is being analysed, each image is treated independently. Astutely, Vasan et al. (2019) use the values of tension at each edge and pressure in each cell from the previous time point as an initial guess for the current time point (see below, in the 'Validations' section, a justification for this method). This informs the inversion method and slightly improves its robustness against noise. They call this 'dynamic local intercellular tension estimation' (DLITE). However, this is still a static method where each inversion is performed on a single image. This is not to be confused with the truly dynamic methods, as discussed in 'Dynamic stress inference'.

Fourth, for experienced users, to solve the inversion problem in that variant, we refer to Noll et al. (2020) who have implemented a useful technical improvement of both the segmentation and inference. Elegantly, they use a so-called 'variational method' to simultaneously

Development (2021) 148, dev192773. doi:10.1242/dev.192773

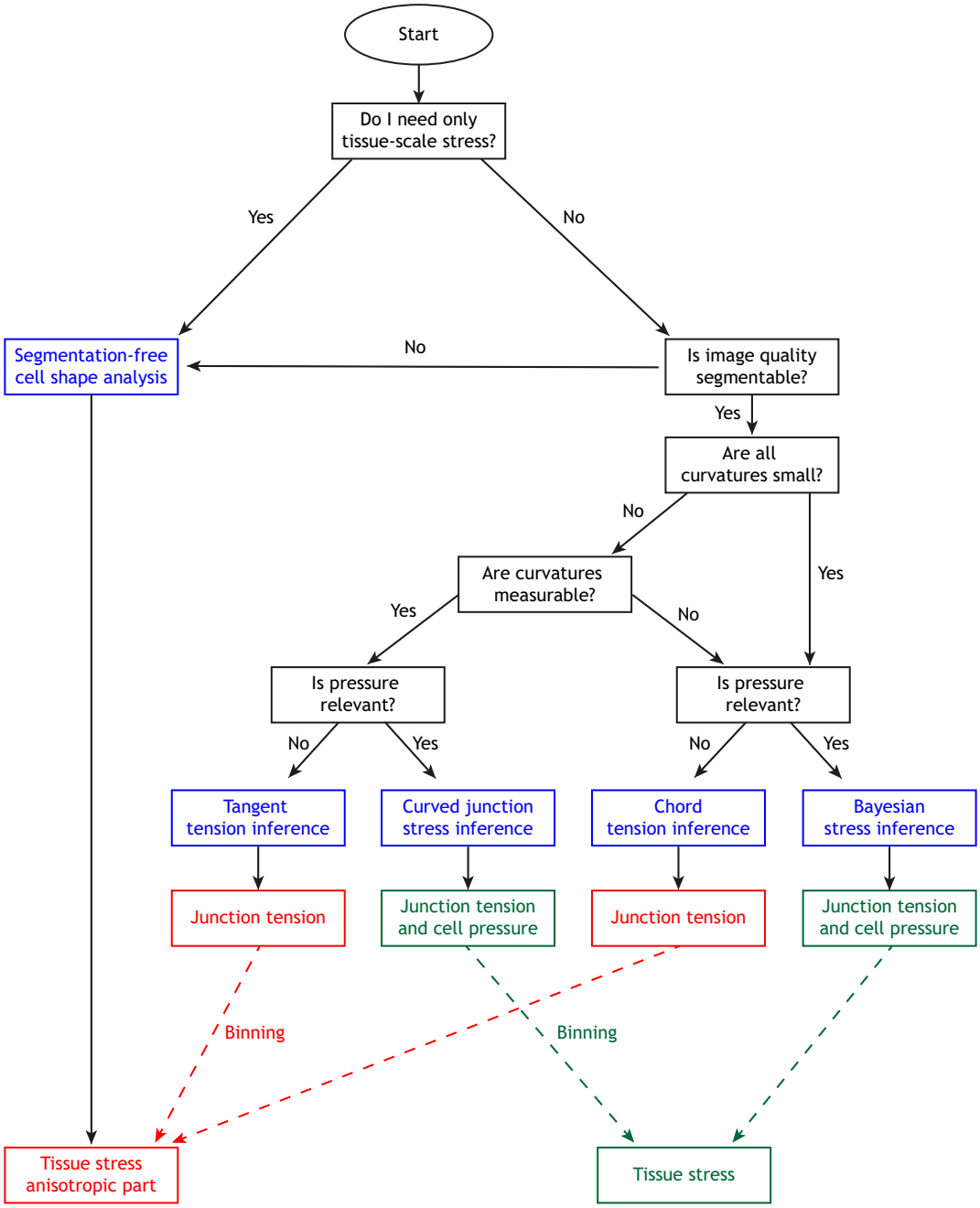

Fig. 5. Flowchart of the various steps involved in choosing the appropriate stress inference variant (blue boxes). Cell stress can be coarse-grained (dashed lines) to provide the tissue stress anisotropic part (red boxes) or full information (green boxes).

determine the angles and curvatures, tensions and pressures that best fit the image: this method together segments the image and infers stresses.

Bayesian stress inference

As opposed to the three above variants, which are overdetermined and solved by a deterministic method, the fourth variant [called Bayesian force inference in Mashburn (2015)] is what we call Bayesian stress inference. It is useful when pressures are required but curvatures cannot be measured precisely, e.g. if the size or contrast of cell contours is insufficient. The number of equations is two per vertex, around $4N$, and the number of unknowns is also around $4N$. In practice, as boundary cells provide incomplete information and fourfold vertices provide more unknowns than equations, the actual number of equations is smaller than the number of unknowns: the problem is 'underdetermined' and cannot be solved in the same way as the approaches described above. Instead, Bayesian methods (see Glossary, Box 1) (Akaike, 1980; Kaipio and Somersalo, 2004) have been applied by Ishihara, Sugimura and co-workers (Ishihara and Sugimura, 2012; Ishihara et al., 2013; Sugimura and Ishihara, 2013; Sugimura et al., 2013; Guirao et al., 2015) followed by Kong et al. (2019). Several pieces of *a priori* information can be imposed, e.g. all junction tensions are expected to be positive; missing information (e.g. on junction curvature) is statistically restored (Ishihara and Sugimura, 2012).

For experienced users, note that Ishihara and Sugimura (2012) use equations different from Eqns 1 and 2. In fact, as they do not take into

account junction curvatures, they describe the network of junctions as equivalent to a set of rigid rods articulated at vertices. This is counter to classical stress inference intuition but is fundamentally correct.

Tissue stress

In all the above variants, cell stress can be coarse-grained through binning (Fig. 5), according to a formula by Batchelor (1970): it is averaged over a given space scale and/or time scale to generate tissue stress (Ishihara and Sugimura, 2012; Ishihara et al., 2013; Sugimura et al., 2013; Guirao et al., 2015; Nestor-Bergmann et al., 2018; Kong et al., 2019; Noll et al., 2020). The anisotropic component of tissue stress arises from coarse-graining the anisotropic contribution of cell junction tensions (Fig. 1B). The isotropic part of tissue stress arises from coarse-graining together cell pressure and the isotropic contribution of cell junction tensions (Kong et al., 2019). A side advantage of coarse-graining is that the signal-to-noise ratio is improved by the averaging, albeit at the expense of space and/or time resolution. In addition, averaging of binned images over several samples also improves the signal-to-noise ratio (Guirao et al., 2015).

There are cases where tissue stress can be obtained without the need to infer cell tensions or pressures (see left of Fig. 5). The underlying assumption here is that cell shape anisotropy correlates with stress anisotropy (Ishihara et al., 2017; Nestor-Bergmann et al., 2018; Xu et al., 2018); this assumption has been validated on some experimental examples (Durande et al., 2019; Kong et al., 2019). When it is valid, this is convenient because cell shape anisotropy can be extracted using techniques that do not require cell contour segmentation, such as Fourier analysis (Durande et al., 2019).

Validations

A common approach to validate stress inference relies on numerical simulations. Chiou et al. (2012); Ishihara and Sugimura (2012); Ishihara et al. (2013); Kong et al. (2019) use the 2D version of the Surface Evolver (Brakke, 1992), while Brodland et al. (2014); Noll et al. (2020) use other algorithms. Such *in silico* benchmarking proceeds as follows: use simulations to generate an equilibrated pattern of cell shapes with known cell junction tensions and pressures, then feed the stress inference code with the cell shapes only to infer tensions and pressures, then compare these inferred values with the known values. This measures the inference uncertainty. The inference robustness is determined by adding errors or noise to the cell shapes before feeding them to the stress inference code (Brodland et al., 2014).

To experimentally validate stress inference, several publications have used junction laser ablation (see Glossary, Box 1), in which post-ablation initial recoil velocity acts as a proxy for relative junction tension prior to ablation. In a tissue consisting of hundreds or thousands of cells and small junction curvature (junction radius of curvature is much larger than cell size), such as the *Drosophila* embryo, chord tension inference and junction ablation correlate well (Kale et al., 2018); in *Drosophila* pupal wing (Sugimura and Ishihara, 2013), pupal dorsal thorax and embryo germband (Kong et al., 2019), Bayesian stress inference and junction ablation correlate well. With a small number of cells and large junction curvature, such as in *Drosophila* retina ommatidia, curved junction stress inference and junction ablation correlate well (Kong et al., 2019).

Other validations of 2D stress inference have come from evidence of a strong correlation between the inferred stress and measured myosin distribution in *Drosophila* embryos (Kale et al., 2018; Noll et al., 2020) or pupal wing (Sugimura and Ishihara, 2013). The ratio between vinculin and E-cadherin image intensities has been used as a ratiometric readout for the mechanical load at E-cadherin complexes, which was shown to correlate with inferred junction tensions (Kale et al., 2018).

Interestingly, although individual cell junction tension measurements are not always validated, better validation has been obtained with collective measurements. For example, in biomimetic systems (liposomes), histograms of tension distributions demonstrated significant changes of average tension after perturbation (Caorsi et al., 2016). Coarse-graining revealed the presence of anisotropic tissue stress in gastrulating avian embryos and stress gradients in *Drosophila* embryos undergoing germband extension, consistent with tissue ablation that cuts a line through several cells (Kong et al., 2019). Similarly, circular tissue ablation in *Drosophila* pupal dorsal thorax showed a correlation with Bayesian stress inference (Ishihara et al., 2013).

Stress inference has also been shown to be robust in time, despite the fact that time variations of absolute tensions cannot be determined. As expected for slow developmental processes, in a time-lapse movie the inferred relative tensions display small fluctuations with time, of order of minutes (Sugimura et al., 2013). This justifies the method of Vasan et al. (2019) discussed previously.

Low spatial fluctuations can also be a sign of stress inference robustness, visible, for example, in the left-right symmetry of tissue stress with respect to the *Drosophila* pupal thorax midline (Fig. 1B). Mashburn (2015) performed a detailed study of the method's strengths and weaknesses, including its robustness to noise and the uncertainty in detecting large-scale pressure gradients, and calls for more systematic evaluations on various data sets.

For experienced users, internal validations consist of testing the robustness of the inference itself, i.e. how sensitive the inversion problem is to the noise and experimental uncertainties. Among them are residuals and standard errors, which should be systematically checked in overdetermined cases (Brodland et al., 2014; Ehsandar, 2015; Veldhuis et al., 2015; Mashburn, 2015). In underdetermined cases, using Bayesian stress inference, there are specific criteria to check (Ishihara and Sugimura, 2012).

Finally, again for experienced users, there is another important marker for the robustness of inversion. The 'condition number' (see Glossary, Box 1) measures how truly independent the equations are. A large condition number reveals that the inversion problem is ill-posed, even if at first sight it seems overdetermined, while a small condition number indicates that the inversion problem is well-posed and inference is reliable (Brodland et al., 2014; Ehsandar, 2015; Veldhuis et al., 2015; Mashburn, 2015). Readers can refer to the supplementary information for more technical explanation on condition number.

Which variant to use?

The following steps should be considered when applying stress inference to study biological processes. First, one should ask whether the biological question requires the measurement of cell junction tension, of cell pressure, or both. Second, one should consider whether relative measurements of junctional tension or pressure is sufficient for one's purpose, or whether absolute values are required. Third, one should search for strong deviations from equilibrium (Fig. 2). If there are few strong deviations, one can discard them and apply stress inference, depending on the required precision, as discussed by Veldhuis et al. (2015) and Kong et al. (2019). In tissues very far from equilibrium, one should consider other options such as dynamic stress inference (see 'Dynamic stress inference' section).

Each variant has its own merits, depending on the tissue, image quality and the biological question under consideration. Here, we describe the steps (summarized in Fig. 5) involved in choosing the optimal cell stress inference variant, which largely depends on the expected output. Image quality, junction curvature, boundary information, cell number and condition number should also be taken into account, as we now detail.

The first aspect to consider is image quality or, more precisely, the possibility of recognizing all cell contours (segmentability). Are the membrane signals sufficiently good for quantifying angles of junction tangent at vertices? The accuracy of stress inference is highly sensitive to the quality of image segmentation: a single strongly erroneous angle measurement can affect inferred tension values over the entire tissue (Brodland et al., 2014). When detailed information of individual cell shape is not required or when poor image quality or large cell number render segmentation and inference computationally demanding, alternative segmentation-free methods can be considered (Durande et al., 2019).

The choice also depends on whether the junctions are almost straight or significantly curved (Kong et al., 2019; Noll et al., 2020). If the curvatures of all cells are small or barely measurable, then if pressure is not of interest one could proceed directly to chord tension inference; but if one wishes to extract both junction tension and pressure, then Bayesian stress inference will be the optimal choice (Kong et al., 2019). Junctions that are regular arcs of circles with strong curvature, as in the case of *Drosophila* retina ommatidia (Kong et al., 2019), can be treated by the curved junction tension inference; if pressure is not of interest, then tangent tension inference should suffice.

When enough information is available, including on cells located at the tissue boundary, comparison of variants shows that deterministic methods are preferable (Brodland et al., 2014). Conversely, Bayesian stress inference outperforms the others in terms of accuracy and robustness when some information is missing (Ishihara et al., 2013; Sugimura et al., 2013; Brodland et al., 2014).

The cell number varies much in applications of stress inference, typically ranging from a few cells (Xu et al., 2018; Kong et al., 2019) to thousands of cells (Guirao et al., 2015; Kong et al., 2019). In a large tissue where bulk cells largely outnumber the boundary cells, there are many more equations than the unknown parameters (tension and pressure); the problem is overdetermined and is suitable for tangent or chord tension inference (Kong et al., 2019). If pressure is of interest, as curved junction stress is prone to error propagation when the system size increases (Brodland et al., 2014), Bayesian stress inference is recommended (Guirao et al., 2015). For smaller tissues, if each cell is well imaged, tangent or curved junction inference is adequate (Kong et al., 2019); but if the problem is underdetermined, Bayesian stress inference is the natural choice.

Finally, when the condition number is small, the inversion problem is well-posed and overdetermined procedures perform better. When the condition number is large, the inversion problem is ill-posed and Bayesian stress inference is preferable.

From two dimensions to three dimensions

A living tissue is 3D, yet when it is a flat monolayer, stress inference can be applied to the apical adherens junctions that transmit stress from cell to cell, which allows 2D analysis. Even when a tissue is not flat or monolayered, there can be cases where it can be approximated as quasi-2D to allow for 2D stress inference.

For example, for a pair of liposomes (Caorsi et al., 2016), or a few cells (Brodland et al., 2010), a 2D section through a symmetry plane, or a fit of cell shape with a sphere, simplifies the analysis. In 3D monolayered epithelia, such as in *Drosophila* germband (Chiou et al., 2012; Kong et al., 2019; McCleery et al., 2019; Noll et al., 2020), egg chamber (Bellver Arnau, 2015) or pupal dorsal thorax (Ishihara and Sugimura, 2012; Ishihara et al., 2013; Guirao et al., 2015; Kong et al., 2019) (Fig. 1A-D, Table 1), 2D stress inference can be applied to the apical surface, locally approximated by a plane. The method is at its validity limit in the case of *Drosophila* egg chamber, which is nearly spherical.

3D stress inference

History

A first extension of stress inference to 3D was introduced by Ehsandar (2015), who demonstrated in his PhD thesis that the 2D version of CellFIT is not reliable on 3D data. He then developed the first actual 3D stress inference, called CellFIT-3D. Starting from watershed-segmented 3D images, his algorithm took into account the pixel intensity to define edges and triple junctions as precisely as possible. CellFIT-3D was published 2 years later by Veldhuis, Brodland and co-workers in two successive articles, one for method details (Veldhuis et al., 2017) and one for biological application (Krens et al., 2017). In Xu et al. (2018), the segmentation process was identical up to additional smoothing steps, and angles between the cells were extracted using mathematical modelling.

Harmand (2019) compared the same junction tension inferred in the apical plane with that inferred in a sectional view, and found different results. The apparent contradiction vanishes if a 2D line tension contribution is added to the 3D junction tension. This is consistent with theoretical prediction (Hannezo et al., 2014; Bielmeier et al., 2016; Alt et al., 2017) and experimental finding (Bielmeier et al., 2016) of an apical belt contractility. Interestingly, this line tension is measurable; the ratio of line tension to junction tension is a length, found to be 4.5 µm (Harmand, 2019), which is the expected order of magnitude (Hannezo et al., 2014).

Basic principle

In three dimensions, the ratio of the number of measured quantities to unknown quantities is larger than in two dimensions because there are more edges than faces: the inference is therefore more overdetermined. An edge is the line where three cells meet. An edge equilibrium is expressed by Eqn 1 written in any plane perpendicularly intersecting this edge (Fig. 6). Under the hypothesis that all points along the edge are in mechanical equilibrium, the angles used in Eqn 1 can be measured at any of these points, or better by averaging several measurements along the same edge.

In three dimensions, Eqn 2 is written with actual pressures, expressed in Nm^{-2}; junction tensions are 2D tensions expressed in Nm^{-1}. Technically, a 3D surface has two curvature radii R and R' at each point, and it is the so-called 'mean curvature' $K=1/R+1/R'$, expressed in m^{-1}, that enters the right hand side of Eqn 2. At mechanical equilibrium a cell junction has a homogeneous mean curvature K, but as R and R' can separately vary, the junction is not necessarily spherical. This poses a challenge in fitting cell junction shapes, especially as image segmentation is more difficult in three dimensions than in two dimensions.

Validations

All steps of the pipeline, i.e. image segmentation, angle measurements and stress inference, are prone to errors that are inherently larger in three dimensions. On early mouse embryos undergoing compaction at the eight-cell stage, Veldhuis et al. (2017) exemplifies the large uncertainties with angle measurements and CellFIT-3D based stress inference (Ehsandar,

Development (2021) 148, dev192773. doi:10.1242/dev.192773

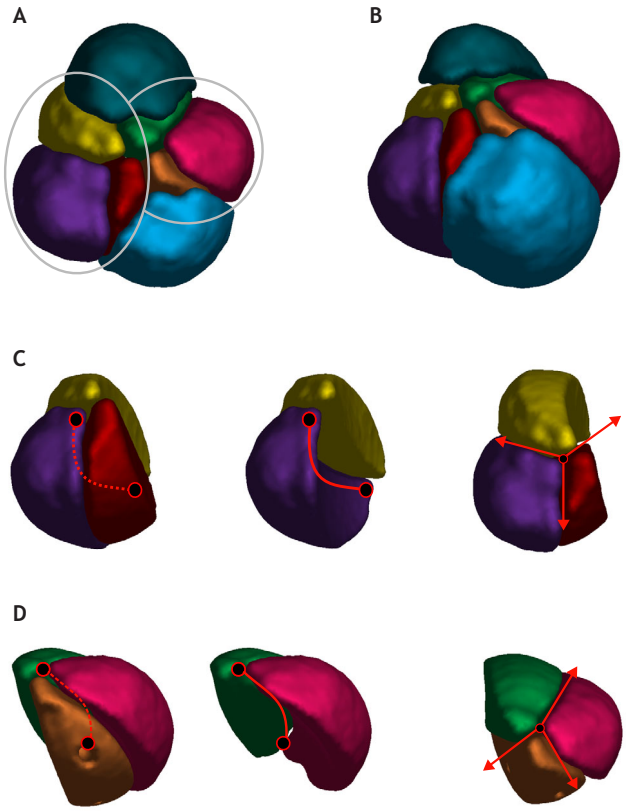

Fig. 6. Principle of stress inference in three dimensions. (A) 3D top view of a mouse embryo. Grey circled regions represent the three-cell systems in C and D. (B) 3D tilted view of the embryo in A. (C) Three cells (left panel) share three junctions, their common edge (dotted line) and its two end vertices (open circles). To better visualize the edge, one segmented cell (red) is removed (middle panel). To measure junction angles, the image is rotated (right panel) and visualizes the 2D section perpendicular to the edge; both vertices are approximately projected on top of each other (not shown). (D) Another example illustrating the same principle of edge detection as in C, in which junction angles strongly differ. Cell sizes are not specified as they are not relevant for stress inference.

2015), as well as with pipette measurements (Maître et al., 2015). In zebrafish, Krens et al. (2017) measured tangent angles to infer junction tensions independently of pressures. High uncertainties could arise from poor image quality and/or non-equilibrated cell shapes. For example, some cells exhibit protrusion-like projections or kinks at the junctions with the other cells (see a comparable example, on a four-cell mouse embryo, in Fig. 2I). This was partially addressed by the manual removal of outliers but could be a case for dynamic stress inference (see section on 'Dynamic stress inference').

Only limited validations have been published. *In silico*, Ehsandar (2015) and Veldhuis et al. (2017) used the 3D version of the Surface Evolver (Brakke, 1992) while Xu et al. (2018) used automated generation of two-cell systems with various angles. Experimental attempts include laser ablation on *Drosophila* embryos (Ratheesh et al., 2018), which provides relative tension values, and micropipette aspiration of zebrafish embryos (Petridou et al., 2019), which provides absolute values of tension.

Assessment

To gain confidence in the validity of 3D stress inference, further tests will be necessary using a larger and more varied data set of tension values, as well as improved image acquisition, segmentation, filtering, cell junction fitting and tangent angle measurement. In the supplementary information, we present a case study for 3D stress inference on preimplantation mouse embryos (eight- and 16-cell stage) and compare the findings with tension measurements using micropipette aspiration.

In brief, we find that stress inference detects regional differences in cell junction tensions, e.g. between the cell-medium tension (outer tension) and the cell-cell tension in early mouse embryos, consistent with measurements by micropipette aspiration. Stress inference also reveals an increase in outer tension with time (from early to late eight-cell stage) or when the outer cells are more stretched [comparing reduced embryos generated from a single blastomere isolated at the four-cell stage and cultured to the 16-cell stage (4/16) with one generated from two blastomeres in the same way (8/16)], consistent with aspiration measurements (Figs S1 and S2) and previous findings (Maître et al., 2015; Chan et al., 2019).

A key question about 3D stress inference is how much error occurs in the inferred tensions due to uncertainty in angle measurements. To illustrate this uncertainty, we choose different combinations of angles compatible with a same well contrasted image of a pseudo-vertex, iterate it on each pseudo-vertex and infer all junction tensions in an 8/16 embryo (Fig. 7). We observe that, although the different choices of angles generate uncertainties in the inferred tension, the average inferred cell-medium tensions t_{cm} for the outer cells (M/OC) are consistently higher than the average cell-cell tensions t_{cc} between two outer cells (OC/OC), one outer and one inner cell (OC/IC), or between two inner cells (IC/IC). This demonstrates that 3D stress inference, on a statistical level, can reasonably tolerate an uncertainty of 10° in the angle measurements.

Extensions

We now propose some extensions and possible improvements in this field.

Polar coordinates

To improve the robustness of stress inference against noise, fluctuations and experimental uncertainty, there is an alternative way to write vertex equations (Harmand, 2019; Noll et al., 2020). It only applies to threefold vertices and can thus be recommended if the proportion of fourfold vertices is small enough. There is a theorem named after Bernard Lami or Lamy (1640-1715) (Thompson, 1917; Clapham and Nicholson, 2009) that states that when the resultant of three vectors is zero, the magnitude of each vector is proportional to the sine of the angle between the directions of the other two vectors. Applied to three tensions, t, at a vertex where the angles between junctions are noted ϕ (Figs 3D and 4B), this yields:

$$\frac{t_1}{\sin\phi_1} = \frac{t_2}{\sin\phi_2} = \frac{t_3}{\sin\phi_3}. \qquad \text{(Eqn 6)}$$

These polar coordinates, more than cartesian coordinates (Eqn 5), reflect the symmetry of the problem, the information provided by the angle measurements, and our intuition (Fig. 4B). In addition, the more angles deviate from 180°, the larger the sines are and the more robust the inference is using Eqn 6.

A further refinement (Harmand, 2019), also for threefold vertices, consists of looking for the unknowns $X = \ln t$ by taking the logarithm of Eqn 6:

$$X_1 - \ln\sin\phi_1 = X_2 - \ln\sin\phi_2 = X_3 - \ln\sin\phi_3. \qquad \text{(Eqn 7)}$$

Development (2021) 148, dev192773. doi:10.1242/dev.192773

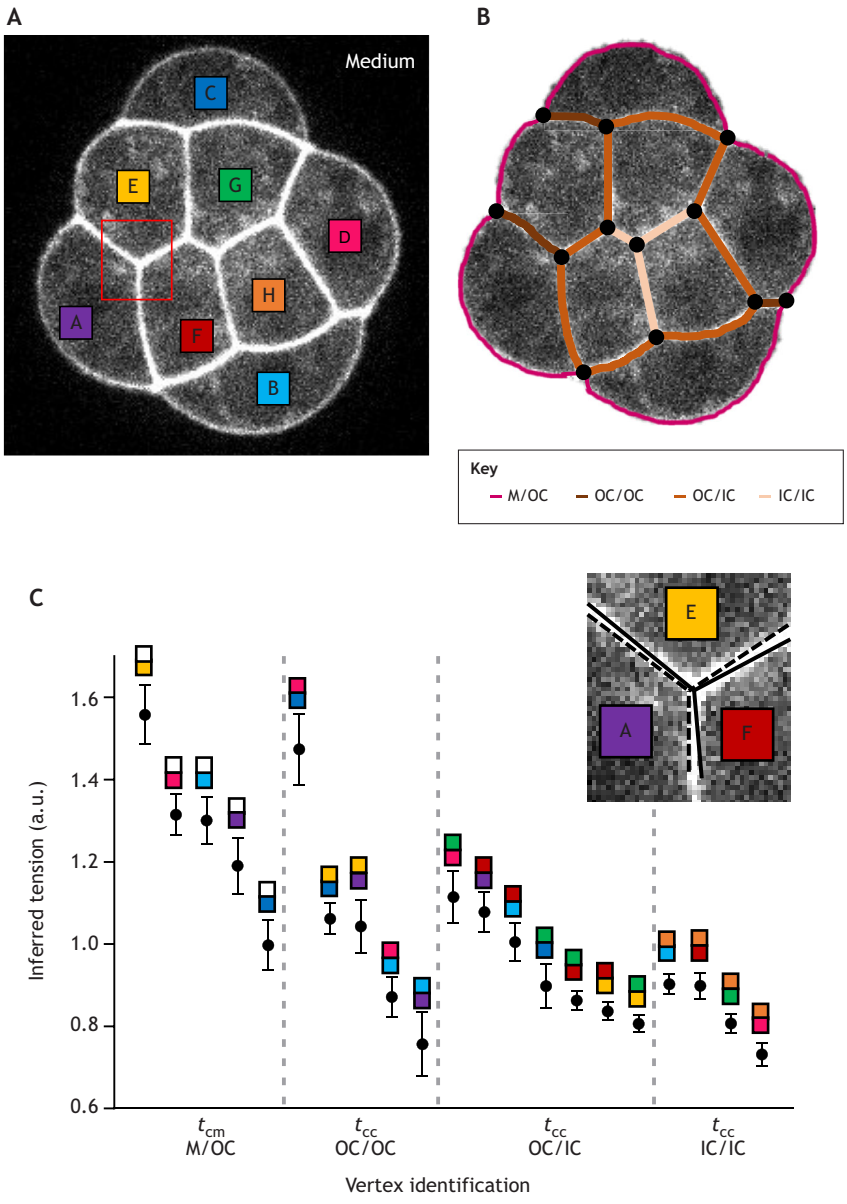

Fig. 7. 3D stress inference is robust against fluctuations due to errors in angle measurements. (A) Image of an 8/16 mouse embryo with fluorescent membrane label ('mTmG'). The outer cells are A-E and the inner cells are F-H. Red box outlines the inset in C. (B) Tensions t_{cm} for the outer cells (M/OC, pink) are plotted separately from cell-cell tensions t_{cc} between two outer cells (OC/OC, brown), between one outer and one inner cell (OC/IC, dark orange), or between two inner cells (IC/IC, light orange). (C) Inset shows higher magnification of the region outlined in A with overlay of two possible different combinations of angles (black lines, dashed black lines) on a 2D section. The 2D section has been chosen as perpendicularly as possible to the edge where three cells meet: it is a pseudo-vertex. Graph shows inferred tensions based on 11 angle combinations at all such pseudo-vertices. Each point is associated with two coloured squares, indicating the specific tension junction measured. Owing to the 3D nature of the structure, not all 11 pseudo-vertices are visible in the 2D slice chosen as an illustration. Data are mean±s.d. Colours correspond to cell colours in A; white indicates medium. Tensions are expressed in arbitrary units; cell sizes are not specified as they are not relevant for stress inference.

This is a linear problem in the unknown X values that can be solved easily; it is always well conditioned and its inversion is robust with few outliers. The average X can be set to zero. Tensions are obtained as $t = \exp X$ and are always positive by construction, which is physically reasonable. Their product is 1 and so is their geometrical average.

Dynamic stress inference

As noted above, one key consideration in using stress inference is whether the tissue is in a quasi-static mechanical equilibrium (Eqns 1 and 2). Readers can refer to the supplementary information for more technical explanation on generalizing these equations to out of equilibrium situations (Viennot and Décamp, 2020). Highly dynamic and out of equilibrium processes may include cell blebbing, periodic cortical waves (Maître et al., 2015) or rapid cell rounding during mitosis. In cases where cell movements are fast, viscous dissipation of the vertices and junctions must be accounted for in the constitutive equations. After addressing several technical challenges in a series of articles (Chen and Brodland, 2000; Brodland et al., 2007; Cranston et al., 2010), Brodland and co-workers have proposed a method to infer, from live movies, an estimate of the junction tensions and cell pressures needed to drive vertex and junction movements. The authors named this method video force microscopy (Brodland et al., 2010; Hutson et al., 2013; Mashburn, 2015); we would call it dynamic stress inference.

Such a method can be useful in analysing morphogenetic movements where cells are driven out of mechanical equilibrium, preferably when images cover the entire tissue, including its boundaries; images covering only a small region of a larger epithelium are more difficult to analyse (Hutson et al., 2013). It has been used to estimate the cell stresses driving invagination on a cross-section of *Drosophila* embryo during gastrulation (Brodland et al., 2010), and to infer the stresses driving *Drosophila* germband retraction and wound healing (Hutson et al., 2013). Other teams have generalized the method to infer the stresses from the velocity field, describing the tissue as a viscous fluid rather than a cellular material (He et al., 2014; Hernández-Vega et al., 2017).

Perspectives in 3D stress inference

Although 2D stress inference has been well developed over the past decade, given that many tissues are intrinsically 3D we foresee a great potential for future development and application of 3D stress inference techniques. These may include validations of 3D stress inference using stress sensors such as liquid droplets for cell-level measurements (Campàs et al., 2014), and deformable gel beads for absolute measurements of tissue stress (Dolega et al., 2017; Mohagheghian et al., 2018; Lee et al., 2019; Träber et al., 2019). Comparison of 3D stress inference with membrane tension sensors (Colom et al., 2018; Li et al., 2018) may present exciting opportunities to study the contribution of cell membrane to cell junction tensions.

With the advance in technology to better quantify cell curvatures in 3D, pressure inference could become readily accessible in a large range of tissues. In principle, it might become possible to generalize to three dimensions the variational method of Noll et al. (2020) to simultaneously segment the image and infer stress, although it might be challenging to fit all cell contours. Finally, segmentation-free methods such as those based on Fourier transform (Durande et al., 2019) could easily be extended to three dimensions to extract coarse-grained cell shape anisotropy and hence 3D tissue stress information.

Conclusions

In this Primer, we provide a comprehensive survey and discussion of the various variants of stress inference, which has gained recent popularity as a novel tool to map cellular tensions and pressures in living tissues. In particular, we focused on the underlying principles and practical considerations for each approach in tackling the different aspects of biological questions. We also look towards future developments in the field that should allow stress inference to be used in a broader range of situations. Such information will prove useful in advancing future applications of stress inference to better understand the roles of mechanics in tissue morphogenesis, homeostasis and diseases.

Acknowledgements

We thank F. Agnès, I. Bonnet, R. Clément and F. Gallet for critical reading of the manuscript, and N. Decamp and L. Viennot for discussions. We thank authors whose work we have cited for providing figures, permission to reproduce them and explanations.

Competing interests

The authors declare no competing or financial interests.

Funding

C.J.C. is supported by H2020 Marie Skłodowska-Curie Actions COFUND (664726) European Molecular Biology Laboratory (EMBL) Interdisciplinary Postdoc (EIPOD). T.H. is supported by the European Molecular Biology Laboratory and the European Research Council (advanced grant 'SelforganisingEmbryo', 742732).

Supplementary information

Supplementary information available online at
https://dev.biologists.org/lookup/doi/10.1242/dev.192773.supplemental

References

Acharya, B. R., Nestor-Bergmann, A., Liang, X., Gupta, S., Duszyc, K., Gauquelin, E., Gomez, G. A., Budnar, S., Marcq, P., Jensen, O. E. et al. (2018). A mechanosensitive RhoA pathway that protects epithelia against acute tensile stress. *Dev. Cell* **47**, 439-452.e6. doi:10.1016/j.devcel.2018.09.016

Akaike, H. (1980). Likelihood and the Bayes procedure. In *Bayesian Statistics* (ed. J. M. Bernardo, M. H. DeGroot, D. V. Lindley and A. F. M. Smith). Valencia: University Press.

Alt, S., Ganguly, P. and Salbreux, G. (2017). Vertex models: from cell mechanics to tissue morphogenesis. *Philos. Trans. R. Soc. Lond. B* **372**, 20150520/1-10. doi:10.1098/rstb.2015.0520

Bardet, P.-L., Guirao, B., Paoletti, C., Serman, F., Léopold, V., Bosveld, F., Goya, Y., Mirouse, V., Graner, F. and Bellaïche, Y. (2013). PTEN controls junction lengthening and stability during cell rearrangement in epithelial tissue. *Dev. Cell* **25**, 534-546. doi:10.1016/j.devcel.2013.04.020

Batchelor, G. K. (1970). The stress system in a suspension of force-free particles. *J. Fluid Mech.* **41**, 545-570. doi:10.1017/S0022112070000745

Bayes, T. and Price, R. (1763). An Essay towards solving a Problem in the Doctrine of Chances. By the late Rev. Mr. Bayes, communicated by Mr. Price, in a letter to John Canton, A. M. F. R. S. *Philos. Trans. R. Soc. Lond.* **53**, 370-418. doi:10.1098/rstl.1763.0053

Bellver Arnau, J. (2015). Morphogenèse cellulaire et apoptose: étude quantitative. *Master thesis*, University Paris Diderot.

Bielmeier, C., Alt, S., Weichselberger, V., La Fortezza, M., Harz, H., Jülicher, F., Salbreux, G. and Classen, A.-K. (2016). Interface contractility between differently fated cells drives cell elimination and cyst formation. *Curr. Biol.* **26**, 563-574. doi:10.1016/j.cub.2015.12.063

Bosveld, F., Guirao, B., Wang, Z., Rivière, M., Bonnet, I., Graner, F. and Bellaïche, Y. (2016). Modulation of junction tension by tumor suppressors and proto-oncogenes regulates cell-cell contacts. *Development* **143**, 623-634. doi:10.1242/dev.127993

Brakke, K. A. (1992). The Surface Evolver. *Exp. Math.* **1**, 141-165. doi:10.1080/10586458.1992.10504253

Brodland, G. W. (2002). The Differential Interfacial Tension Hypothesis (DITH): a comprehensive theory for the self-rearrangement of embryonic cells and tissues. *J. Biomech. Eng* **124**, 188-197. doi:10.1115/1.1449491

Brodland, G. W., Viens, D. and Veldhuis, J. H. (2007). A new cell-based FE model for the mechanics of embryonic epithelia. *CMBBE* **10**, 121-128. doi:10.1080/10255840601124704

Brodland, G. W., Conte, V., Cranston, P. G., Veldhuis, J., Narasimhan, S., Hutson, M. S., Jacinto, A., Ulrich, F., Baum, B. and Miodownik, M. (2010). Video force microscopy reveals the mechanics of ventral furrow invagination in Drosophila. *Proc. Natl. Acad. Sci. USA* **107**, 22111-22116. doi:10.1073/pnas.1006591107

Brodland, G. W., Veldhuis, J. H., Kim, S., Perrone, M., Mashburn, D. and Hutson, M. S. (2014). CellFIT: a cellular force-inference toolkit using curvilinear cell boundaries. *PLoS ONE* **9**, e99116. doi:10.1371/journal.pone.0099116

Campàs, O. (2016). A toolbox to explore the mechanics of living embryonic tissues. *Semin. Cell Dev. Biol.* **55**, 119-130. doi:10.1016/j.semcdb.2016.03.011

Campàs, O., Mammoto, T., Hasso, S., Sperling, R. A., O'Connell, D., Bischof, A. G., Mass, R., Weitz, D. A., Mahadevan, L. and Ingber, D. E. (2014). Quantifying cell-generated mechanical forces within living embryonic tissues. *Nat. Methods* **11**, 183-189. doi:10.1038/nmeth.2761

Cantat, I., Cohen-Addad, Elias, S. F., Graner, F., Höhler, R., Pitois, O., Rouyer, F. and Saint-Jalmes, A. (2013). *Foams: Structure and Dynamics* (ed. S. J. Cox). Oxford University Press.

Caorsi, V., Lemière, J., Campillo, C., Bussonnier, M., Manzi, J., Betz, T., Plastino, J., Carvalho, K. and Sykes, C. (2016). Cell-sized liposome doublets reveal active tension build-up driven by acto-myosin dynamics. *Soft Mat.* **12**, 6223-6231. doi:10.1039/C6SM00856A

Carter, R., Sánchez-Corrales, Y. E., Hartley, M., Grieneisen, V. A. and Marée, A. F. M. (2017). Pavement cells and the topology puzzle. *Development* **144**, 4386-4397. doi:10.1242/dev.157073

Chan, C. J., Heisenberg, C.-P. and Hiiragi, T. (2017). Coordination of morphogenesis and cell-fate specification in development. *Curr. Biol.* **27**, R1024-R1035. doi:10.1016/j.cub.2017.07.010

Chan, C. J., Costanzo, M., Ruiz-Herrero, T., Mönke, G., Petrie, R. J., Bergert, M., Diz-Muñoz, A., Mahadevan, L. and Hiiragi, T. (2019). Hydraulic control of mammalian embryo size and cell fate. *Nature* **571**, 112-116. doi:10.1038/s41586-019-1309-x

Chen, H. H. and Brodland, G. W. (2000). Cell-level finite element studies of viscous cells in planar aggregates. *J. BioMech. Eng.* **122**, 394-401. doi:10.1115/1.1286563

Chiou, K. K., Hufnagel, L. and Shraiman, B. I. (2012). Mechanical stress inference for two dimensional cell arrays. *PLoS Comput. Biol.* **8**, e1002512. doi:10.1371/journal.pcbi.1002512

Clapham, C. and Nicholson, J. (2009). *The Concise Oxford Dictionary of Mathematics*. Oxford: Oxford University Press.

Colom, A., Derivery, E., Soleimanpour, S., Tomba, C., Molin, M. D., Sakai, N., González-Gaitán, M., Matile, S. and Roux, A. (2018). A fluorescent membrane tension probe. *Nat. Chem.* **10**, 1118-1125. doi:10.1038/s41557-018-0127-3

Cranston, P. G., Veldhuis, J. H., Narasimhan, S. and Brodland, G. W. (2010). Cinemechanometry (CMM): A method to determine the forces that drive morphogenetic movements from time-lapse images. *Ann. Biomed. Eng.* **38**, 2937-2947. doi:10.1007/s10439-010-9998-1

Dolega, M. E., Delarue, M., Ingremeau, F., Prost, J., Delon, A. and Cappello, G. (2017). Cell-like pressure sensors reveal increase of mechanical stress towards the core of multicellular spheroids under compression. *Nat. Commun.* **8**, 14056. doi:10.1038/ncomms14056

Dupont, J.-C. (2017). Wilhelm His and mechanistic approaches to development at the time of Entwicklungsmechanik. *Hist. Philos. Life Sci.* **39**, 21. doi:10.1007/s40656-017-0148-z

Durande, M., Tlili, S., Homan, T., Guirao, B., Graner, F. and Delanoë-Ayari, H. (2019). Fast determination of coarse-grained cell anisotropy and size in epithelial tissue images using Fourier transform. *Phys. Rev. E* **99**, 062401/1–10. doi:10.1103/PhysRevE.99.062401

Ehsandar, A. (2015). Inferring 3D Cellular Forces from Confocal Image Stacks. *PhD thesis*, University of Waterloo, Canada..

Fujita, M. and Onami, S. (2012). Cell-to-cell heterogeneity in cortical tension specifies curvature of contact surfaces in Caenorhabditis elegans embryos. *PLoS ONE* **7**, e30224. doi:10.1371/journal.pone.0030224

Gjorevski, N. and Nelson, C. M. (2010). The mechanics of development: models and methods for tissue morphogenesis. *Birth Defects Res. C* **90**, 193-202. doi:10.1002/bdrc.20185

Gómez-González, M., Latorre, E., Arroyo, M. and Trepat, X. (2020). Measuring mechanical stress in living tissues. *Nat. Rev. Phys.* **2**, 300-317. doi:10.1038/s42254-020-0184-6

Graner, F. and Riveline, D. (2017). The forms of tissues, or cell-aggregates: D'Arcy Thompson's influence and its limits. *Development* **144**, 4226-4237. doi:10.1242/dev.151233

Guirao, B., Rigaud, S. U., Bosveld, F., Bailles, A., López-Gay, J., Ishihara, S., Sugimura, K., Graner, F. and Bellaïche, Y. (2015). Unified quantitative characterization of epithelial tissue development. *eLife* **4**, e08519/1–52. doi:10.7554/eLife.08519

Hannezo, E. and Heisenberg, C.-P. (2019). Mechanochemical feedback loops in development and disease. *Cell* **178**, 12-25. doi:10.1016/j.cell.2019.05.052

Hannezo, E., Prost, J. and Joanny, J.-F. (2014). Theory of epithelial sheet morphology in three dimensions. *Proc. Natl. Acad. Sci. USA* **111**, 27-32. doi:10.1073/pnas.1312076111

Harmand, N. (2019). Pertinence et limites des tensions de surface et de ligne pour rendre compte des formes de cellules épithéliales. *PhD thesis*, University of Paris, France. https://hal.archives-ouvertes.fr/tel-02892746.

He, B., Doubrovinski, K., Polyakov, O. and Wieschaus, E. (2014). Apical constriction drives tissue-scale hydrodynamic flow to mediate cell elongation. *Nature* **508**, 392-396. doi:10.1038/nature13070

Heer, N. C. and Martin, A. C. (2017). Tension, contraction and tissue morphogenesis. *Development* **144**, 4249-4260. doi:10.1242/dev.151282

Heisenberg, C.-P. and Bellaïche, Y. (2013). Forces in tissue morphogenesis and patterning. *Cell* **153**, 948-962. doi:10.1016/j.cell.2013.05.008

Hernández-Vega, A., Marsal, M., Pouille, P. A., Tosi, S., Colombelli, J., Luque, T., Navajas, D., Pagonabarraga, I. and Martín-Blanco, E. (2017). Polarized cortical tension drives zebrafish epiboly movements. *EMBO J.* **36**, 25-41. doi:10.15252/embj.201694264

His, W. (1874). *Unsere Körperform und das physiologische Problem ihrer Entstehung*. Leipzig: F. C. W. Vogel.

Hutson, M. S., Mashburn, D., Copenhaver, E., McCleery, W. T., Veldhuis, J., Kim, S. and Brodland, G. W. (2013). In-plane video force microscopy of morphogenesis in epithelia. In *American Physical Society* **58**, G44.004 http://meetings.aps.org/link/BAPS.2013.MAR.G44.4.

Ishihara, S. and Sugimura, K. (2012). Bayesian inference of force dynamics during morphogenesis. *J. theor. Biol.* **313**, 201-211. doi:10.1016/j.jtbi.2012.08.017

Ishihara, S., Sugimura, K., Cox, S. J., Bonnet, I., Bellaïche, Y. and Graner, F. (2013). Comparative study of non-invasive force and stress inference methods in tissue. *Eur. Phys. J. E* **36**, 45. doi:10.1140/epje/i2013-13045-8

Ishihara, S., Marcq, P. and Sugimura, K. (2017). From cells to tissue: a continuum model of epithelial mechanics. *Phys. Rev. E* **96**, 022418. doi:10.1103/PhysRevE.96.022418

Käfer, J., Hayashi, T., Marée, A. F. M., Carthew, R. W. and Graner, F. (2007). Cell adhesion and cortex contractility determine cell patterning in the Drosophila retina. *Proc. Natl. Acad. Sci. USA* **104**, 18549-18554. doi:10.1073/pnas.0704235104

Kaipio, J. and Somersalo, E. (2004). *Statistical and Computational Inverse Problems*. New York: Springer.

Kale, G. R., Yang, X., Philippe, J.-M., Mani, M., Lenne, P.-F. and Lecuit, T. (2018). Distinct contributions of tensile and shear stress on E-cadherin levels during morphogenesis. *Nat. Commun.* **9**, 5021. doi:10.1038/s41467-018-07448-8

Kong, W., Loison, O., Shivakumar, P. C., Chan, E. H. Y., Saadaoui, M., Collinet, C., Lenne, P.-F. and Clément, R. (2019). Experimental validation of force inference in epithelia from cell to tissue scale. *Sci. Rep.* **9**, 14647. doi:10.1038/s41598-019-50690-3

Krens, S. F. G., Veldhuis, J. H., Barone, V., Čapek, D., Maître, J.-L., Brodland, G. W. and Heisenberg, C.-P. (2017). Interstitial fluid osmolarity modulates the action of differential tissue surface tension in progenitor cell segregation during gastrulation. *Development* **144**, 1798-1806. doi:10.1242/dev.144964

Lamiré, L.-A., Milani, P., Runel, G., Kiss, A., Arias, L., Vergier, B., de Bossoreille, S., Das, P., Cluet, D., Boudaoud, A. and Grammont, M. (2020). Gradient in cytoplasmic pressure in germline cells controls overlying epithelial cell morphogenesis. *PLoS Biol. 18, e3000940*. https://doi.org/10.1371/journal.pbio.3000940.

Landsberg, K. P., Farhadifar, R., Ranft, J., Umetsu, D., Widmann, T. J., Bittig, T., Said, A., Jülicher, F. and Dahmann, C. (2009). Increased cell bond tension governs cell sorting at the Drosophila anteroposterior compartment boundary. *Curr. Biol.* **19**, 1950-1955. doi:10.1016/j.cub.2009.10.021

Lecuit, T. and Lenne, P.-F. (2007). Cell surface mechanics and the control of cell shape, tissue patterns and morphogenesis. *Nat. Rev. Mol. Cell Biol.* **8**, 633-644. doi:10.1038/nrm2222

Lee, W., Kalashnikov, N., Mok, S., Halaoui, R., Kuzmin, E., Putnam, A. J., Takayama, S., Park, M., McCaffrey, L., Zhao, R. et al. (2019). Dispersible hydrogel force sensors reveal patterns of solid mechanical stress in multicellular spheroid cultures. *Nat. Commun.* **10**, 144. doi:10.1038/s41467-018-07967-4

Li, W., Yu, X., Xie, F., Zhang, B., Shao, S., Geng, C., Aziz, A. U. R., Liao, X. and Liu, B. (2018). A membrane-bound biosensor visualizes shear stress-induced inhomogeneous alteration of cell membrane tension. *iScience* **7**, 180-190. doi:10.1016/j.isci.2018.09.002

Maître, J.-L., Niwayama, R., Turlier, H., Nédélec, F. and Hiiragi, T. (2015). Pulsatile cell-autonomous contractility drives compaction in the mouse embryo. *Nat. Cell Biol.* **17**, 849-855. doi:10.1038/ncb3185

Mammoto, A., Mammoto, T. and Ingber, D. E. (2012). Mechanosensitive mechanisms in transcriptional regulation. *J. Cell Sci.* **125**, 3061-3073. doi:10.1242/jcs.093005

Mashburn, D. N. (2015). Mapping Developmental Mechanics in Drosophila melanogaster with Segmentation and Force Inference. *PhD thesis*, Vanderbilt University, USA.

McCleery, W. T., Veldhuis, J., Bennett, M. E., Lynch, H. E., Ma, X., Brodland, G. W. and Hutson, M. S. (2019). Elongated cells drive morphogenesis in a surface-wrapped finite-element model of germband retraction. *Biophys. J.* **117**, 157-169. doi:10.1016/j.bpj.2019.05.023

Miller, C. J. and Davidson, L. A. (2013). The interplay between cell signalling and mechanics in developmental processes. *Nat. Rev. Gen.* **14**, 733-744. doi:10.1038/nrg3513

Mohagheghian, E., Luo, J., Chen, J., Chaudhary, G., Chen, J., Sun, J., Ewoldt, R. H. and Wang, N. (2018). Quantifying compressive forces between living cell layers and within tissues using elastic round microgels. *Nat. Commun.* **9**, 1878. doi:10.1038/s41467-018-04245-1

Nestor-Bergmann, A., Goddard, G., Woolner, S. and Jensen, O. E. (2018). Relating cell shape and mechanical stress in a spatially disordered epithelium using a vertex-based model. *Math. Med. Biol.* **35** Suppl. 1, 1-27. doi:10.1093/imammb/dqx008

Neumann, N. M., Perrone, M. C., Veldhuis, J. H., Huebner, R. J., Zhan, H., Devreotes, P. N., Brodland, G. W. and Ewald, A. J. (2018). Coordination of receptor tyrosine kinase signaling and interfacial tension dynamics drives radial intercalation and tube elongation. *Dev. Cell* **45**, 67-82.e6. doi:10.1016/j.devcel.2018.03.011

Noll, N., Streichan, S. J. and Shraiman, B. I. (2020). Variational method for image-based inference of internal stress in epithelial tissues. *Phys. Rev. X* **10**, 011072. doi:10.1103/PhysRevX.10.011072

Ouchi, N. B., Glazier, J. A., Rieu, J.-P., Upadhaya, A. and Sawada, Y. (2003). Improving the realism of the cellular Potts model in simulations of biological cells. *Physica A* **329**, 451-458. doi:10.1016/S0378-4371(03)00574-0

Petridou, N. I., Grigolon, S., Salbreux, G., Hannezo, E. and Heisenberg, C.-P. (2019). Fluidization-mediated tissue spreading by mitotic cell rounding and non-canonical Wnt signalling. *Nat. Cell Biol.* **21**, 169-178. doi:10.1038/s41556-018-0247-4

Ratheesh, A., Biebl, J., Vesela, J., Smutny, M., Papusheva, E., Krens, S. F. G., Kaufmann, W., Gyoergy, A., Casano, A. M. and Siekhaus, D. E. (2018). Drosophila TNF modulates tissue tension in the embryo to facilitate macrophage invasive migration. *Dev. Cell* **45**, 331-346.e7. doi:10.1016/j.devcel.2018.04.002

Rauzi, M., Verant, P., Lecuit, T. and Lenne, P.-F. (2008). Nature and anisotropy of cortical forces orienting Drosophila tissue morphogenesis. *Nat. Cell Biol.* **10**, 1401-1410. doi:10.1038/ncb1798

Roca-Cusachs, P., Conte, V. and Trepat, X. (2017). Quantifying forces in cell biology. *Nat. Cell Biol.* **19**, 742-751. doi:10.1038/ncb3564

Samarage, C. R., White, M. D., Álvarez, Y. D., Fierro-González, J. C., Henon, Y., Jesudason, E. C., Bissiere, S., Fouras, A. and Plachta, N. (2015). Cortical tension allocates the first inner cells of the mammalian embryo. *Dev. Cell* **34**, 435-447. doi:10.1016/j.devcel.2015.07.004

Spencer, M. A., Jabeen, Z. and Lubensky, D. K. (2017). Vertex stability and topological transitions in vertex models of foams and epithelia. *Eur. Phys. J. E* **40**, 2. doi:10.1140/epje/i2017-11489-4

Stein, M. B. and Gordon, R. (1982). Epithelia as bubble rafts: a new method for analysis of cell shape and intercellular adhesion in embryonic and other epithelia. *J. theor. Biol.* **97**, 625-639. doi:10.1016/0022-5193(82)90363-0

Sugimura, K. and Ishihara, S. (2013). The mechanical anisotropy in a tissue promotes ordering in hexagonal cell packing. *Development* **140**, 4091-4101. doi:10.1242/dev.094060

Sugimura, K., Bellaïche, Y., Graner, F., Marcq, P. and Ishihara, S. (2013). Robustness of force and stress inference in an epithelial tissue. *IEEE Eng. Med. Biol. Soc.* 2712-2715. doi:10.1109/EMBC.2013.6610100

Sugimura, K., Lenne, P.-F. and Graner, F. (2016). Measuring forces and stresses in situ in living tissues. *Development* **143**, 186-196. doi:10.1242/dev.119776

Taylor, J. E. (1976). The structure of singularities in soap-bubble-like and soap-film-like minimal surfaces. *Ann. Math.* **103**, 489-539. doi:10.2307/1970949

Thompson, D. W. (1917). *On Growth and Form*, enlarged edn 1942. Cambridge, UK: Cambridge University Press.

Träber, N., Uhlmann, K., Girardo, S., Kesavan, G., Wagner, K., Friedrichs, J., Goswami, R., Bai, K., Brand, M., Werner, C. et al. (2019). Polyacrylamide bead sensors for in vivo quantification of cell-scale stress in Zebrafish development. *Sci. Rep.* **9**, 17031. doi:10.1038/s41598-019-53425-6

Vasan, R., Maleckar, M. M., Williams, C. D. and Rangamani, P. (2019). DLITE uses cell-cell interface movement to better infer cell-cell tensions. *Biophys. J.* **117**, 1714-1727. doi:10.1016/j.bpj.2019.09.034

Veldhuis, J. H., Mashburn, D., Hutson, M. S. and Brodland, G. W. (2015). Practical aspects of the cellular force inference toolkit (CellFIT). *Meth. Cell Biol.* **125**, 331-351. doi:10.1016/bs.mcb.2014.10.010

Veldhuis, J. H., Ehsandar, A., Maître, J.-L., Hiiragi, T., Cox, S. and Brodland, G. W. (2017). Inferring cellular forces from image stacks. *Philos. Trans. R. Soc. Lond. B* **372**, 20160261. doi:10.1098/rstb.2016.0261

Viennot, L. and Décamp, N. (2020). *Developing Critical Thinking in Physics*. Dordrecht: Springer (ESERA series).

White, J. L. (1964). Dynamics of viscoelastic fluids, melt fracture, and the rheology of fiber spinning. *J. Appl. Polymer Sci.* **8**, 2339-2357. doi:10.1002/app.1964.070080527

Xiong, F., Ma, W., Hiscock, T. W., Mosaliganti, K. R., Tentner, A. R., Brakke, K. A., Rannou, N., Gelas, A., Souhait, L., Swinburne, I. A. et al. (2014). Interplay of cell shape and division orientation promotes robust morphogenesis of developing epithelia. *Cell* **159**, 415-427. doi:10.1016/j.cell.2014.09.007

Xu, M., Wu, Y., Shroff, H., Wu, M. and Mani, M. (2018). A scheme for 3-dimensional morphological reconstruction and force inference in the early C. elegans embryo. *PLoS ONE* **13**, e0199151. doi:10.1371/journal.pone.0199151

Yang, J. and Brodland, G. W. (2009). Estimating interfacial tension from the shape histories of cells in compressed aggregates: A computational study. *Ann. Biomed. Eng.* **37**, 1019-1027. doi:10.1007/s10439-009-9649-6

Supplementary information

TECHNICAL EXPLANATIONS

For experienced users we develop two technical points alluded to in the main text.

Regarding condition number

Imagine one is solving two equations with two unknowns (a, b). In the mathematical plane (a, b), each equation has solutions represented by a line, and the solution of the system is the point (a_0, b_0) where these lines intersect. If at (a_0, b_0) both lines are nearly perpendicular to each other, it means that the equations provide really independent information, and the solution (a_0, b_0) is determined with precision and robustness. When the lines representing the equations intersect with a very acute angle, they are not truly independent, and the value of (a_0, b_0) is sensitive to the exact positioning of the lines, to noise and to solver errors. The condition number generalises that idea to several equations with many unknowns (Brodland et al., 2014; Ehsandar, 2015; Veldhuis et al., 2015; Mashburn, 2015).

Regarding out of equilibrium situations

To generalise Eqs. (1,2) to out of equilibrium situations, it helps to understand their origin. These equations do not result from Newton's second law of motion, that of inertia, which applies to systems with a mass. Here the vertices and junctions have a negligible mass, and whether they are accelerated or not does not change the mechanical balance. In fact, Eqs. (1,2) result from Newton's third law of motion, namely the equality of action and reaction (here between cell contour and cytoplasm), which always holds, whether at or out of equilibrium (Viennot and Décamp, 2020). In out of equilibrium situations, the equations should include dissipative interactions such as arising from viscosity.

ASSESSMENT ON MOUSE EMBRYOS OF 3D STRESS INFERENCE PIPELINE

To assess the various steps of the pipeline used in practice, here we conducted 3D stress inference and micropipette aspiration on preimplantation mouse embryos (8- and 16-cell stage). Pipettes can measure tensions of contact surfaces between outer cells and the medium, hereafter noted t_{cm} and called *outer tension* for brevity. We first analysed the images (Fig. S1a) presented in Veldhuis et al. (2017). Our procedure (Fig. 7) consists in manually segmenting cells, then rotating the reconstructed embryo to visualize a section perpendicular to each three-cell edge, and extract angles; tensions are then automatically inferred. We inferred a consistently higher outer tension t_{cm} compared to the cell-cell tension $t_{cc}/2$ at 90 min and 240 min post division during compaction (Fig. S1b). This difference between t_{cm} and $t_{cc}/2$ increased with time during compaction, consistent with previous study (Maître et al., 2015). We found no correlation between pipette tension and inferred tension between individual cells in the same embryo (Fig. S1c). This could be due to the small range of measured tension in the same embryo that is too small to be resolved with the stress inference detection precision. Alternatively, we note that the micropipette aspiration itself incurs some experimental errors. The resolution of the applied pressure in the setup is about 10 Pa, which translates to an error of pipette tension in the range of 30 to 50 pN/μm. This could generate the intra-embryo variability in pipette tension in Fig. S1c.

We next studied the outer tension of "reduced embryos" (Maître et al., 2015; Chan et al., 2019). Briefly, embryos at the 4-cell stage were washed with pronase to remove the *zona pellucida*. The embryos were then washed in calcium-free medium, and the dissociated blastomeres (1/4 embryos) were cultured to reach the 16-cell stage, which we term the 4/16 embryos. Similarly, 8/16 embryos were made by aggregating two dissociated blastomeres at the 4-cell stage and cultured to reach the 16-cell stage.

Performing stress inference on these reduced embryos, we inferred consistently higher outer tensions compared to cell-cell tensions, for both the 4/16 and 8/16 embryos (Fig. S1d, h), consistent with the case of full embryos (Maître et al., 2015). This demonstrates that 3D stress inference can detect region-specific differences in tension within a tissue, at different developmental stages and with different cell geometries.

We observed a better correlation between pipette tension and inferred tension in the 8/16 embryos (Fig. S1i) than in the 4/16 embryos (Fig. S1f). This could be due to the too small range of pipette tensions in the 4/16 embryos. We had previously shown that the outer tension correlates with cell stretching in early mouse embryos (Chan et al., 2019). Hence, the small variability of pipette tensions in 4/16 embryos may be due to the fact that the outer cells in these embryos are more equally stretched (Fig. S1e) while those of the 8/16 embryos are stretched to various different degrees (Fig. S1g).

We had previously shown that the reduced embryos have higher outer tensions compared to that of the full embryos, due to the cells being more stretched (Chan et al., 2019). We therefore investigated whether this trend can be captured by 3D stress inference. Indeed, we inferred a higher outer tension (normalised to the cell-cell tension) in the 4/16 embryos, compared to that of the 8/16 embryos (Fig. S2b). This is consistent with the measured pipette tensions (Fig. S2a), which further validates the robustness of 3D stress inference on a statistical level.

Journal of Experimental Biology • Supplementary information

Supplementary Figures

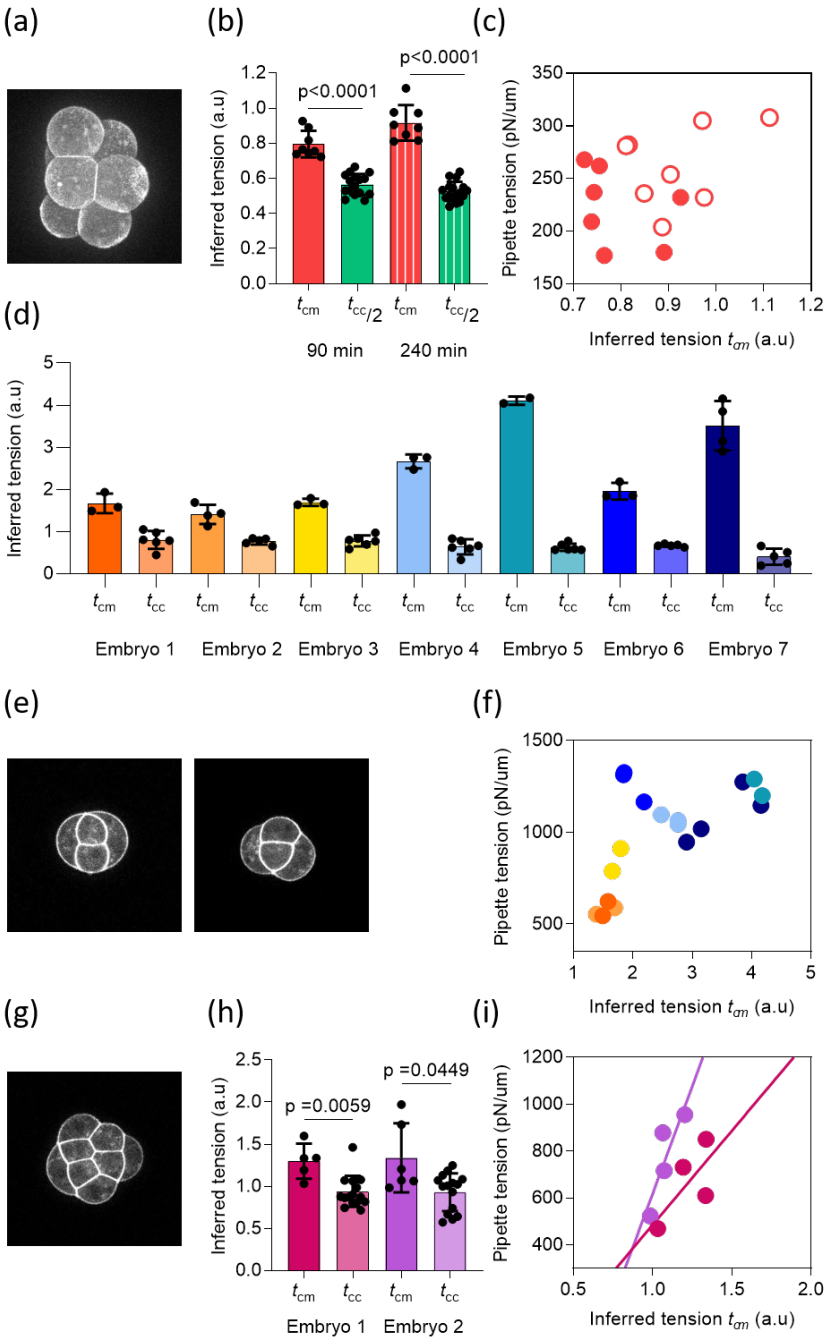

Fig. S1. Stress inference detects spatial and temporal changes of tension in early mouse embryos on a statistical level. (a) 8-cell stage mTmG mouse embryo. (b) Plot of inferred outer tensions t_{cm} and cell-cell tensions t_{cc} between inner cells at 90 min and 240 min post division time (8-cell stage). One embryo per timepoint was analyzed, containing each 8 cells with 21 junctions each. (c) Plot shows a lack of correlation between measured and inferred outer tensions in the same embryo measured at early (close circles) and late (open circles) 8-cell stage. (d) Plot of inferred outer tensions and cell-cell tensions in 4/16 embryos. Stress inference can detect the difference between the two tensions in the same embryo. 7 embryos were analyzed, containing each 4 cells which represent between 9 and 11 junctions per embryo. (e) 4/16 mTmG embryos. (f) Plot shows a lack of correlation between the measured and inferred outer tensions within the same 4/16 embryo. Each curve corresponds to one embryo, pipette tension was measured for 2, 3 or 4 cells per embryo according to their accessibility. (g) 8/16 mTmG embryos. (h) Plot of outer tensions and cell-cell tensions in 8/16 embryos. Stress inference again detects the difference between tensions in the same embryo. Two embryos were analyzed, with 8 cells and 21 junctions per embryo. (i) Plot shows a correlation between the measured and inferred outer tensions within the same 8/16 embryo.

Journal of Experimental Biology • Supplementary information

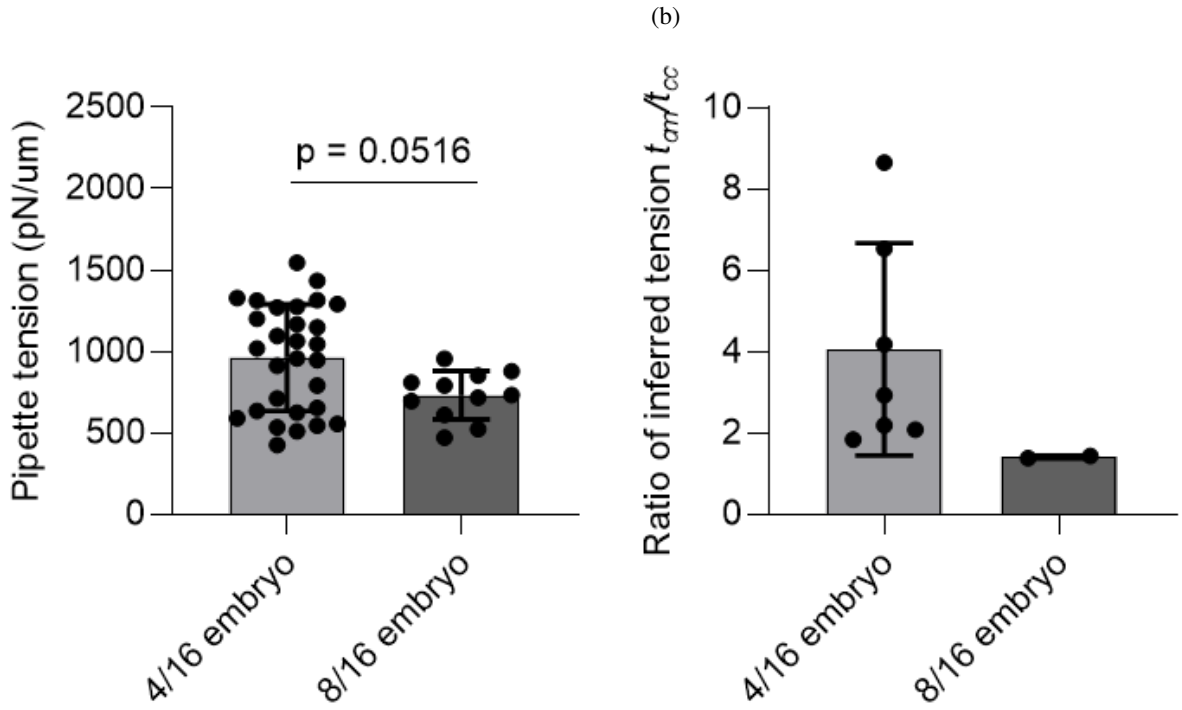

Fig. S2. 4/16 mouse embryos have higher outer tensions compared to that of 8/16 embryos, as measured by micropipettes (a) and inferred by stress inference (b). In (b), each data point indicates the average outer tension t_{cm} normalised to the average cell-cell tension t_{cc} per embryo. 4/16 embryos: 28 cells and 63 interfaces in 7 embryos; 8/16 embryos: 16 cells and 65 junctions in 2 embryos.